

JUL 08 1983

DEC 20 1983

FEB 02 1984

AFWAL-TR-83-2002
Volume II

ROTATING STALL INVESTIGATIONS
VOLUME II - EXPERIMENTAL STUDIES



Aerodynamic Research Department
Arvin/Calspan Advanced Technology Center
P.O. Box 400
Buffalo, New York 14225

Property of U. S. Air Force
AEDC LIBRARY
F40600-81-C-0004

January 1983

TECHNICAL REPORTS
FILE COPY

Final Report for Period 15 August 1979 - 15 October 1982

Approved for public release; distribution unlimited

Aero Propulsion Laboratory
AIR FORCE WRIGHT AERONAUTICAL LABORATORIES
AIR FORCE SYSTEMS COMMAND
WRIGHT-PATTERSON AIR FORCE BASE, OHIO 45433

NOTICE

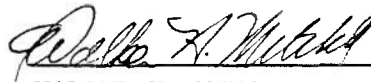
When Government drawings, specifications, or other data are used for any purpose other than in connection with a definitely related Government procurement operation, the United States Government thereby incurs no responsibility nor any obligation whatsoever; and the fact that the government may have formulated, furnished, or in any way supplied the said drawings, specifications, or other data, is not to be regarded by implication or otherwise as in any manner licensing the holder or any other person or corporation, or conveying any rights or permission to manufacture use, or sell any patented invention that may in any way be related thereto.

This report has been reviewed by the Office of Public Affairs (ASD/PA) and is releasable to the National Technical Information Service (NTIS). At NTIS, it will be available to the general public, including foreign nations.

This technical report has been reviewed and is approved for publication.



MARVIN A. STIBICH
Compressor Technology Group
Technology Branch



WALKER H. MITCHELL
Chief, Technology Branch
Turbine Engine Division

FOR THE COMMANDER



H. I. BUSH, Director
Turbine Engine Division
Aero Propulsion Laboratory

"If your address has changed, if you wish to be removed from our mailing list, or if the addressee is no longer employed by your organization please notify AFWAL/POTX, W-PAFB, OH 45433 to help us maintain a current mailing list".

Copies of this report should not be returned unless return is required by security considerations, contractual obligations, or notice on a specific document.

SECURITY CLASSIFICATION OF THIS PAGE (When Data Entered)

REPORT DOCUMENTATION PAGE		READ INSTRUCTIONS BEFORE COMPLETING FORM
1. REPORT NUMBER AFWAL-TR-83-2002, Vol. II	2. GOVT ACCESSION NO.	3. RECIPIENT'S CATALOG NUMBER
4. TITLE (and Subtitle) Rotating Stall Investigations Volume II - Experimental Studies		5. TYPE OF REPORT & PERIOD COVERED Final Report for Period 15 Aug 1979-15 Oct 1982
		6. PERFORMING ORG. REPORT NUMBER 6568-A-6
7. AUTHOR(s) G. R. Ludwig and J. P. Nenni		8. CONTRACT OR GRANT NUMBER(s) F33615-79-C-2023
9. PERFORMING ORGANIZATION NAME AND ADDRESS Aerodynamic Research Department Arvin/Calspan Advanced Technology Center P.O. Box 400, Buffalo, New York 14225		10. PROGRAM ELEMENT, PROJECT, TASK AREA & WORK UNIT NUMBERS 3066/04/55
11. CONTROLLING OFFICE NAME AND ADDRESS Aero Propulsion Laboratory (AFWAL/POTX) Air Force Wright Aeronautical Laboratories (AFSC) Wright-Patterson Air Force Base, Ohio 45433		12. REPORT DATE January 1983
		13. NUMBER OF PAGES 310
14. MONITORING AGENCY NAME & ADDRESS (if different from Controlling Office)		15. SECURITY CLASS. (of this report) Unclassified
		15a. DECLASSIFICATION/DOWNGRADING SCHEDULE
16. DISTRIBUTION STATEMENT (of this Report) Approved for public release; distribution unlimited.		
17. DISTRIBUTION STATEMENT (of the abstract entered in Block 20, if different from Report)		
18. SUPPLEMENTARY NOTES		
19. KEY WORDS (Continue on reverse side if necessary and identify by block number) Rotating Stall Fluid Mechanics Compressors Jet Engines Unsteady Aerodynamics		
20. ABSTRACT (Continue on reverse side if necessary and identify by block number) This report presents the results of a research program on rotating stall in axial flow compressors and jet engines. The program had three major objectives which were: (1) develop an analysis for a three-dimensional, time-variant rotating stall and separation theory, (2) develop analysis for post-stall operation/recovery and aerodynamically induced exotic metal combustion and (3) consider the effects of distortion, water ingestion, and nuclear blasts on axial flow compressors. The work done towards accomplishing		

20. (continued)

objective (1) is reported in Volume I. The work done towards the accomplishment of the remaining two objectives is reported in Volume II presented herein. The experimental studies were performed on a low-speed rotating annular cascade facility and on a J-85-5 turbojet engine. The low-speed tests investigated the influence of rotor-stator interference on the work performed by a rotor in a stage prior to and during rotating stall, both with and without inlet distortion. The J-85 experiments consisted of post-stall temperature measurements in the compressor and a demonstration of stall anticipation and stall recovery on this engine with a previously developed rotating stall control system in operation. In addition, some blast tests were performed on the J-85 with the stall control system both operative and inoperative. Comparisons are made between the low-speed experimental results and the predictions of a previously developed two-dimensional rotating stall stability theory. In addition, post-stall analyses were performed on both the low-speed results and the J-85 results for comparison with the predictions of Day, Greitzer, and Cumpsty.

FOREWORD

This is the final technical report prepared by Calspan Corporation on a portion of a multi-phase program sponsored by the Air Force Aeropropulsion Laboratory, Air Force Systems Command, Wright-Patterson Air Force Base, Ohio, under Contract F33615-79-C-2023. The work reported herein was performed as part of Project 3066, "Rotating Stall Investigations", with Mr. Marvin A. Stibich, AFWAL/POTX, as Project Engineer. Dr. Gary R. Ludwig of the Aerodynamic Research Department of Arvin/Calspan Advanced Technology Center, had overall technical responsibility for the program, and carried out the experimental measurements. The theoretical studies of rotating stall were performed by Dr. Joseph P. Nenni and Dr. Gregory F. Homicz.

TABLE OF CONTENTS

<u>Section</u>		<u>Page</u>
I	INTRODUCTION	1
II	STUDIES IN ROTATING ANNULAR CASCADE	4
	1. INTRODUCTION	4
	2. DESCRIPTION OF ANNULAR CASCADE FACILITY	6
	a. General Description	6
	b. Instrumentation	9
	c. Determination of Bearing Tare Torque	10
	3. ISOLATED ROTOR	11
	a. Inlet Flow Calibration	11
	b. Velocity Field Downstream of Isolated Rotor..	14
	c. Integrated Velocity Components and Comparisons With Other Measurements	17
	d. Rotor Torque, Total Pressure Rise, and Loss Coefficients	21
	4. ROTOR-STATOR STAGE	26
	a. Rotor Torque	26
	b. Total Pressure Distribution on Rotor	27
	c. Axial Velocity and Mass Flow Weighted Total Pressure Rise Distributions	29
	d. Rotor Torque, Total Pressure Rise and Loss Coefficients	31
	e. Tests With Inlet Distortion.....	36
	5. STABILITY AND POST-STALL ANALYSES	38
	a. Application of Stability Theory	38
	b. Post-Stall Analysis of Annular Cascade Data..	41

TABLE OF CONTENTS (Contd.)

<u>Section</u>		<u>Page</u>
III	J-85 ENGINE TESTS	50
	1. INTRODUCTION	50
	2. INSTRUMENTATION	51
	3. ROTATING STALL CONTROL TESTS	52
	a. Time Available to Effect Stall Recovery	53
	b. Stall Anticipation	58
	4. THIN-FILM TEMPERATURE MEASUREMENTS DURING ROTATING STALL	62
	a. Thin-Film Temperature-Time Histories	63
	b. Analysis of Temperature Records	68
	5. STALL CONTROL BLAST TESTS	74
	6. POST-STALL ANALYSIS OF J-85 DATA	77
IV	SUMMARY AND CONCLUSIONS	84
	REFERENCES	89
	APPENDIX A: HOT-FILM ANEMOMETER DATA ANALYSIS	207
	APPENDIX B: COMPUTER PRINTOUTS OF VELOCITY AND TOTAL PRESSURE DISTRIBUTIONS	237
	APPENDIX C: WATER INGESTION	284

LIST OF ILLUSTRATIONS

<u>Figure</u>		<u>Page</u>
1	Low Hub-to-Tip Ratio Annular Cascade With Torque Meter	91
2	Torque On Sealed Rotor	92
3	Radial Distribution of Total Pressure Coefficient Far Upstream of Rotor	93
4	Radial Distributions of Velocity Components Far Upstream of Rotor	
	(a) Rotor RPM = 500	94
	(b) Rotor RPM = 900	95
	(c) Rotor RPM = 1200	96
5	Radial Distributions of Mean Velocity Components Downstream of Isolated Rotor	
	(a) Rotor RPM = 400	97
	(b) Rotor RPM = 600	98
	(c) Rotor RPM = 800	99
	(d) Rotor RPM = 900	100
	(e) Rotor RPM = 950	101
	(f) Rotor RPM = 1000	102
	(g) Rotor RPM = 1050	103
	(h) Rotor RPM = 1100	104
	(i) Rotor RPM = 1300	105
6	Dimensionless RMS Velocity Components Downstream of Isolated Rotor	
	(a) Rotor RPM = 400, 500, 600, 700	106
	(b) Rotor RPM = 800, 850, 900	107

LIST OF ILLUSTRATIONS (Cont'd)

<u>Figure</u>		<u>Page</u>
6	(c) Rotor RPM = 950, 1000	108
	(d) Rotor RPM = 1050, 1100	109
	(e) Rotor RPM = 1200, 1300	110
7	Comparison of Swirl Angles Measured by Conrad Arrowhead Probe with Swirl Angles Calculated from Triple Probe Mean Velocity Data	
	(a) Distance from Hub, $\Delta r = 0.91$ and 3.16 in.	111
	(b) Distance from Hub, $\Delta r = 5.41$ and 7.66 in.	112
8	Area Weighted Integrals of Dimensionless Mean Axial Flow Velocity	113
9	Comparison of Rotor Torque Coefficients Calculated from Triple Probe Data with Those Calculated from Torque Meter Data	114
10	Comparisons of Radial Distributions of Mass Flow Weighted Total Pressure Rise Across Isolated Rotor with Rotor Torque Coefficient	
	(a) Rotor RPM = 400, 500	115
	(b) Rotor RPM = 600, 700	116
	(c) Rotor RPM = 800, 850	117
	(d) Rotor RPM = 900, 950	118
	(e) Rotor RPM = 1000	119
	(f) Rotor RPM = 1050	120
	(g) Rotor RPM = 1100	121
	(h) Rotor RPM = 1200	122
	(i) Rotor RPM = 1300	123
11	Averaged Torque, Total Pressure Rise, and Loss Coefficients on Low Hub-Tip Ratio Isolated Rotor	124
12	Comparison of Rotor Torque Coefficients Measured on Isolated Rotor and on the Same Rotor in a Rotor-Stator Stage	125

LIST OF ILLUSTRATIONS (Cont'd)

<u>Figure</u>		<u>Page</u>
13	Radial Distributions of Total Pressure Coefficient Immediately Downstream of Isolated Rotor and the Same Rotor in Rotor-Stator Stage. Stator Stagger Angle at Mean Radius, $\delta_s = 12.9$ deg.	
	(a) Rotor RPM = 400, 500	126
	(b) Rotor RPM = 600, 700	127
	(c) Rotor RPM = 800, 850	128
	(d) Rotor RPM = 900, 950	129
	(e) Rotor RPM = 1000	130
	(f) Rotor RPM = 1050	131
	(g) Rotor RPM = 1100	132
	(h) Rotor RPM = 1200	133
	(i) Rotor RPM = 1300	134
14	Radial Distributions of Total Pressure Coefficient Immediately Downstream of Isolated Rotor and the Same Rotor in Rotor-Stator Stage. Stator Stagger Angle at Mean Radius, $\delta_s = 32.9$ deg.	
	(a) Rotor RPM = 400, 500	135
	(b) Rotor RPM = 600, 700	136
	(c) Rotor PRM = 800, 850	137
	(d) Rotor RPM = 900, 950	138
	(e) Rotor RPM = 1000	139
	(f) Rotor RPM = 1050	140
	(g) Rotor RPM = 1100	141
	(h) Rotor RPM = 1200	142
	(i) Rotor RPM = 1300	143

LIST OF ILLUSTRATIONS (Cont'd)

<u>Figure</u>		<u>Page</u>
15	Radial Distributions of Axial Velocity and Mass Flow Weighted Total Pressure Rise Downstream of Isolated Rotor and the Same Rotor in a Rotor-Stator Stage	
(a)	Rotor RPM = 500	144
(b)	Rotor RPM = 600	145
(c)	Rotor RPM = 700	146
(d)	Rotor RPM = 800	147
(e)	Rotor RPM = 900	148
(f)	Rotor RPM = 1000	149
(g)	Rotor RPM = 1100	150
(h)	Rotor RPM = 1200	151
(i)	Rotor RPM = 1300	152
16	Area Weighted Integrals of Dimensionless Mean Axial Flow Velocity	153
17	Comparison of Area Averaged and Mass-Flow Averaged Total Pressure Rise Across Rotor	154
18	Torque Coefficient and Area-Averaged Total Pressure Rise, and Loss Coefficients for Rotor in Low Hub/Tip Ratio Rotor-Stator Stage. Stator Stagger Angle at Mean Radius $\delta_S = 12.9$ deg.	155
19	Torque Coefficient and Area-Averaged Total Pressure Rise, and Loss Coefficients for Rotor in Low Hub/Tip Ratio Rotor-Stator Stage. Stator Stagger Angle at Mean Radius, $\delta_S = 22.9$ deg. ..	156
20	Torque Coefficient and Area-Averaged Total Pressure Rise, and Loss Coefficients for Rotor in Low Hub/Tip Ratio Rotor-Stator Stage. Stator Stagger Angle at Mean Radius, $\delta_S = 32.9$ deg. ...	157
21	Rotor Torque Coefficients for A Rotor-Stator Stage With and Without Inlet Distortion	
(a)	Stator Stagger Angle, $\delta_S = 12.9$ deg.	158
(b)	Stator Stagger Angle, $\delta_S = 22.9$ deg.	159

LIST OF ILLUSTRATIONS (Cont'd)

Figure		Page
21	(c) Stator Stagger Angle, $\delta_s = 32.9$ deg.	160
22	Stability of Low Hub/Tip Isolated Rotor	161
23	Stability of Rotor in Low Hub/Tip Ratio Rotor-Stator Stage Stator Stagger Angle at Mean Radius, $\delta_s = 12.9$ deg.	162
24	Stability of Rotor in Low Hub/Tip Ratio Rotor Stator Stage Stator Stagger Angle at Mean Radius, $\delta_s = 22.9$ deg.	163
25	Stability of Rotor in Low Hub/Tip Ratio Rotor-Stator Stage Stator Stagger Angle at Mean Radius, $\delta_s = 32.9$ deg.	164
26	Inlet Total to Exit Average Static Pressure Rise Performance of High Hub-to-Tip Ratio Stage in Annular Cascade	165
27	Inlet Total to Exit Axial-Flow Static Pressure Rise Performance of High Hub-to-Tip Ratio Isolated Rotor and Rotor-Stator Stage	166
28	Inlet Total to Exit Axial-Flow Static Pressure Rise Performance of Low Hub-to-Tip Ratio Isolated Rotor and the Same Rotor in a Rotor-Stator Stage	167
29	Cross Section of J-85 Compressor Casing Showing Axial Locations of Pressure Transducers and Thin Film Temperature Probes	168
30	Detail of Thin Film Temperature Probes Used in J-85 Engine	169
31	J-85 Compressor Response to Rotating Stall at Nominal Engine Speed of 70%	
	(a) Integrator Gain = 800; Corrected Engine Speed at Stall Inception, $(N/N^* \sqrt{\theta}) = 69.8\%$	170
	(b) Integrator Gain = 400; Corrected Engine Speed at Stall Inception, $(N/N^* \sqrt{\theta}) = 70.8\%$	171
	(c) Integrator Gain = 200; Corrected Engine Speed at Stall Inception, $(N/N^* \sqrt{\theta}) = 71.1\%$	172
	(d) Integrator Gain = 100; Corrected Engine Speed at Stall Inception, $(N/N^* \sqrt{\theta}) = 71.1\%$	173
32	J-85 Compressor Response to Rotating Stall at Nominal Engine Speed of 75%	
	(a) Integrator Gain = 800; Corrected Engine Speed at Stall Inception, $(N/N^* \sqrt{\theta}) = 75.2\%$	174

LIST OF ILLUSTRATIONS (Cont'd)

<u>Figure</u>		<u>Page</u>
32	(b) Integrator Gain = 400; Corrected Engine Speed at Stall Inception, $(N/N^* \sqrt{\theta}) = 75.0\%$	175
	(c) Integrator Gain = 200; Corrected Engine Speed at Stall Inception, $(N/N^* \sqrt{\theta}) = 74.9\%$	176
	(d) Integrator Gain = 100; Corrected Engine Speed at Stall Inception, $(N/N^* \sqrt{\theta}) = 75.5\%$	177
33	J-85 Compressor Response to Rotating Stall at Nominal Engine Speed of 78%	
	(a) Integrator Gain = 800; Corrected Engine Speed at Stall Inception, $(N/N^* \sqrt{\theta}) = 77.7\%$	178
	(b) Integrator Gain = 200; Corrected Engine Speed at Stall Inception, $(N/N^* \sqrt{\theta}) = 78.7\%$	179
34	J-85 Compressor Response to Rotating Stall at Nominal Engine Speed of 70% (Expanded Time Scale)	
	(a) Integrator Gain = 800; Corrected Engine Speed at Stall Inception, $(N/N^* \sqrt{\theta}) = 69.8\%$	180
	(b) Integrator Gain = 400; Corrected Engine Speed at Stall Inception, $(N/N^* \sqrt{\theta}) = 70.8\%$	181
	(c) Integrator Gain = 200; Corrected Engine Speed at Stall Inception, $(N/N^* \sqrt{\theta}) = 71.1\%$	182
	(d) Integrator Gain = 100; Corrected Engine Speed at Stall Inception, $(N/N^* \sqrt{\theta}) = 71.1\%$	183
35	J-85 Compressor Response to Rotating Stall at Nominal Engine Speed of 75% (Expanded Time Scale)	
	(a) Integrator Gain = 800; Corrected Engine Speed at Stall Inception, $(N/N^* \sqrt{\theta}) = 75.2\%$	184
	(b) Integrator Gain = 400; Corrected Engine Speed at Stall Inception, $(N/N^* \sqrt{\theta}) = 75.0\%$	185
	(c) Integrator Gain = 200; Corrected Engine Speed at Stall Inception, $(N/N^* \sqrt{\theta}) = 74.9\%$	186
	(d) Integrator Gain = 100; Corrected Engine Speed at Stall Inception, $(N/N^* \sqrt{\theta}) = 75.5\%$	187

LIST OF ILLUSTRATIONS (Cont'd)

<u>Figure</u>		<u>Page</u>
36	J-85 Compressor Response to Rotating Stall at Nominal Engine Speed of 78% (Expanded Time Scale)	
(a)	Integrator Gain = 800; Corrected Engine Speed at Stall Inception, $(N/N^* \sqrt{\theta}) = 77.7\%$	188
(b)	Integrator Gain = 200; Corrected Engine Speed at Stall Inception, $(N/N^* \sqrt{\theta}) = 78.8\%$	189
37	J-85 Compressor Parameters Prior to Rotating Stall. Stall Control Detuned to Allow Stall. Corrected Engine Speed at Stall Inception $(N/N^* \sqrt{\theta}) = 70.1\%$	190
38	J-85 Compressor Parameters Prior to Rotating Stall. Stall Control Adjusted to Almost Prevent Stall. Corrected Engine Speed at Stall Inception $(N/N^* \sqrt{\theta}) = 70.5\%$	191
39	Unsteady Temperature Measurements in J-85 Compressor During Rotating Stall	
(a)	Corrected Engine Speed at Stall Inception, $(N/N^* \sqrt{\theta}) = 71.1\%$	192
(b)	Corrected Engine Speed at Stall Inception, $(N/N^* \sqrt{\theta}) = 75.5\%$	193
(c)	Corrected Engine Speed at Stall Inception, $(N/N^* \sqrt{\theta}) = 78.7\%$	194
40	Unsteady Temperature Measurements in J-85 Compressor During Rotating Stall (Expanded Time Scale)	
(a)	Corrected Engine Speed at Stall Inception, $(N/N^* \sqrt{\theta}) = 71.1\%$	195
(b)	Corrected Engine Speed at Stall Inception, $(N/N^* \sqrt{\theta}) = 75.5\%$	196
(c)	Corrected Engine Speed at Stall Inception, $(N/N^* \sqrt{\theta}) = 78.7\%$	197
41	Correlation Between Temperature and Total Pressure Fluctuations in J-85 Compressor During Rotating Stall. Corrected Engine Speed at Stall Inception, $(N/N^* \sqrt{\theta}) = 74.6\%$	198
42	Assumed Model for Heat Transfer Rate During Rotating Stall	199

LIST OF ILLUSTRATIONS (Cont'd)

<u>Figure</u>		<u>Page</u>
43	Comparison Between Experimental and Theoretical Probe Temperature	200
44	Sketch of Shock-Tube Instrumentation	201
45	J-85 Compressor Response to Incident Shock Wave. Stall Control Active. Corrected Engine Speed $N/N^* \sqrt{\theta} = 64.4\%$	202
46	J-85 Post-Stall Behavior	
(a)	Stall Inception at $N/N^* \sqrt{\theta} = 0.72$	203
(b)	Stall Inception at $N/N^* \sqrt{\theta} = 0.76$	204
(c)	Stall Inception at $N/N^* \sqrt{\theta} = 0.79$	205

LIST OF TABLES

<u>Table</u>	<u>Title</u>	<u>Page</u>
1	Geometric Characteristics of Rotor Blades and Stator Vanes.....	8
2	Unmodified Post-Stall Analysis of Day, Greitzer and Cumpsty Applied to Annular Cascade Data.....	44
3	Comparison of Modified Post-Stall Analysis of Day, Greitzer, and Cumpsty With Annular Cascade Results.....	47
4	Summary of Pre-Stall and Stalled Temperature Data During Long Duration Rotating Stalls.....	65

SECTION I

INTRODUCTION

The optimum performance of a turbo-propulsion system is usually achieved when the compressor is operating near its maximum pressure ratio. However, this optimum is generally not attainable because it occurs close to compressor stall and unstable flow conditions. In actual operation, a stall margin must be provided to prevent the compressor from penetrating the stall boundary and developing destructive unsteady flow phenomena such as rotating stall and surge. This is usually done by prescheduling the engine controls. When an aircraft has a varied flight envelope, the prescheduling approach can lead to the requirement for a large stall margin to keep the engine out of stall under all possible transient and steady flight conditions. This stall margin represents a significant performance penalty. Also, in many instances of engine failure, rotating stall has been identified as a precursor to destructive unsteady flows in an engine. Furthermore, blade fatigue considerations will not allow a compressor to operate for prolonged periods in a large amplitude rotating stall mode. Clearly then, it is desirable to develop methods of estimating the stall boundaries of a compressor and if possible to develop an engine control system that can sense incipient destructive unsteady flows in a compressor and take corrective action to prevent compressor stall. Recognition of these goals has been the motivation for a continuing program of research that the AFAPL has sponsored at Calspan since 1962. The last program at Calspan was carried out under Contract No. F33615-76-C-2092 and the results are reported in References 1 through 3.

The work at Calspan has been both theoretical and experimental in nature and has been aimed at obtaining a sufficient understanding of the rotating stall phenomenon such that its onset and its properties can be predicted and controlled. Demonstrated progress has been made toward these goals in that a theory has been developed which is capable of predicting inception of rotating stall on a high hub-to-tip ratio compressor stage (rotor plus stator) in low speed flows, provided that the appropriate steady state blade row performance

data are available. In addition, a prototype rotating stall control system has been designed and demonstrated successfully by tests conducted by Calspan on a J85-5 turbojet engine and by the Air Force Aero Propulsion Laboratory on a J85-13 turbojet engine.

The latest three-year program has the objectives of (1) develop an analysis for a three-dimensional time-variant rotating stall and separation theory, (2) develop analyses for post-stall operation/recovery and aerodynamically induced exotic metal combustion and (3) consider the effects of distortion, water ingestion, and nuclear blasts on axial flow compressors. The work done towards accomplishing objective (1) is reported in Volume I of this report. The work done towards the accomplishment of the remaining objectives are reported herein.

The approach adopted towards accomplishing objectives (2) and (3) listed above was primarily experimental in nature. Experiments in a low-speed rotating annular cascade were performed to investigate the influence of rotor-stator interference on the work performed by a rotor in a compressor stage with and without inlet distortion and during stall. The experiments were performed on a configuration of the annular cascade with low hub-to-tip ratio. They included detailed total pressure surveys, three-component hot-film surveys to determine velocities, and measurement of the torque input to the rotor. Experiments on a J-85 engine with stall control system were performed to study the unsteady temperature fluctuations in the J-85 compressor during rotating stall, the performance of the stall control in anticipating and preventing rotating stall, and the performance requirements for the stall control to clear rotating stall once it has started. Separate tests were performed to study the response of the rotating stall control system when a simulated blast wave impinges on the engine inlet. Analyses of the post-stall behavior were performed for both the low speed annular cascade and the J-85 engine. Finally, a review of the literature applicable to water ingestion effects on a turbojet engine was performed.

The experimental studies in the low speed annular cascade are covered in Section II of this report. Section III presents the results of the tests on the J-85 turbojet engine. A summary of the results and conclusions reached is presented in Section IV. A detailed description of calibration and data analysis techniques used with the three-sensor hot-film probe is presented in Appendix A and tabulated three-component velocity data obtained with this probe are presented in Appendix B. The literature review for water ingestion effects is presented in Appendix C.

SECTION II

STUDIES IN ROTATING ANNULAR CASCADE

1. INTRODUCTION

As a part of the work under a previous program Contract AF33(615)-3357, an annular cascade facility was designed and fabricated. Its principal purpose is to provide detailed fundamental experimental data during and prior to the occurrence of rotating stall in order to improve our understanding of the phenomena and for use as a guide in improving theoretical analyses. The facility has also been used to evaluate the operation of a prototype rotating stall control system (Ref. 4) and to provide acoustic data for comparison with theory (Refs. 2 and 5). This section presents the results of fundamental experiments in the annular cascade to study interference effects on a rotor-stator stage.

Experimental studies on rotor-stator interference have been performed previously in the Calspan/Air Force annular cascade in a configuration with a hub-to-tip ratio of 0.8 (Ref. 3). This investigation included measurements on an isolated rotor, a closely coupled rotor-stator stage, and the same stage with circumferential inlet distortion. The experiments on the stage were performed for two different stagger angle settings of the stators. With undistorted flow, it was found that the presence of the stators delayed rotating stall inception over that which occurs on the isolated rotor. Moreover, prior to rotating stall inception, there was significantly more total pressure rise across the rotor with the stator behind it than there was across the isolated rotor. This could be due to either: (a) the rotor-stator interference produces more rotor work than the isolated case, or (b) the rotor-stator interference produces a reduction in the rotor losses (presumably by influencing boundary layer separation). An attempt was made to resolve these possibilities by measuring the total temperature rise across the rotor. However, the results were not accurate enough to provide reliable estimates of the work done by the rotor.

The experimental steady-state performance data measured on the isolated rotor and on the stage were used to provide inputs to a two-dimensional rotating stall stability theory. The inputs required by the theory are the relative losses and the turning of the flow through the rotor and the losses and turning of the flow through the stators. Calculation of the relative losses through the rotor in the stage required determination of the total pressure rise across the rotor and of the work done by the rotor. As noted above, attempts to measure the rotor work through total temperature measurements were not successful. However, the work done by the isolated rotor had been determined previously through an extensive series of velocity measurements. Thus for application of the stability theory, it was assumed that the work done by the rotor in the stage was the same as that done by the isolated rotor. This corresponds to assuming that the observed increase in total pressure rise across the rotor in the stage is a result of reduced losses through the rotor. With this input, the resulting stability boundary predictions from the theory agreed extremely well with the experimental stall inception boundary for the stage for both stator stagger angles that were tested. However, this result is not conclusive proof as to which effect, more rotor work or reduced rotor losses, is the cause of the significant increase in total pressure rise across the rotor when the stator is placed behind it. Resolving this point is an important factor for rotating stall research as well as for general compressor design practice. Furthermore, inspection of the isolated rotor work measured after rotating stall had started suggested that the presence of rotating stall does not affect the time-averaged rotor work if the mean and velocity in the annular cascade is held constant. If this result is true in general, it may have application towards explaining stall-induced titanium combustion in compressors.

The current work was designed to extend the experimental studies of rotor-stator coupling to determine the effect on rotor work prior to rotating stall inception and during rotating stall. The studies were performed on a low hub-to-tip ratio (0.44) configuration of the annular cascade so that the results could also be used to test the predictions of the rotating stall stability theory for such a case. Previous tests of the stability theory had all been for configurations with high hub-to-tip ratio. Rotor work was determined by measuring the torque input to the rotor during the tests.

The order of presentation of the experimental studies in the annular cascade is as follows. A description of the low hub-to-tip ratio configuration of the annular cascade with a torque measuring device is presented in Section II-B. Section II-C presents the results of measurements on the isolated rotor. Results of measurements on the rotor-stator stage are presented and compared with the isolated rotor measurements in Section II-D. Finally, in Section II-E, the experimental results are compared to the predictions of the stability theory and to those of a post-stall theory developed by Day, Greitzer and Cumpsty (Ref. 6).

2. DESCRIPTION OF ANNULAR CASCADE FACILITY

a. General Description

The annular cascade facility consists of a test section built around the outer front casing of a J-79 jet-engine compressor with a Calspan fabricated hub. The facility includes a bell-mouth inlet on the outer casing and a bullet nose on the hub to provide a smooth flow of air to the test section. Outlet ducting is connected to an independently variable source of suction to provide the required flow through the annulus. An electrically powered two-speed axial flow fan is used as the source of suction. Continuous control of the mass flow is achieved through the use of variable inlet guide vanes to the fan and a variable damper in the fan exit flow. A sketch of the annular cascade facility with a torquemeter on the rotor drive shaft is shown in Fig. 1.

The test section of the annular cascade forms a circular annulus with an outer diameter of 29.4 inches and an inner diameter of 12.8 inches which provides a hub-to-tip ratio of 0.44. The outer casing will accept up to six variable stagger angle stator rows. The hub was designed to accept the first stage rotor from a J-79 compressor at its normal axial location relative to the J-79 outer casing. This allows tests with the rotor alone, or with a stage consisting of the J-79 first stage rotor and first stage stator. The hub has an elliptical nose fairing at the front of the annulus, and the outer casing has the same bell mouth inlet as was used for the high hub-to-tip ratio configuration of Ref. 3.

The rotor uses the original rotor hub section from the J-79 compressor to retain the blades. The original tapered hub was changed to a constant area design by filling the inter-blade spaces on the hub of the rotor blades. The tapered-end stator blades were converted to constant area by trimming the hub ends to the desired shape. The configuration of the stator blade hub-end fittings was retained to allow use of the original stator hub support ring from the J-79 compressor. The final hub-to-tip ratio (0.44) of the new configuration was governed by the radial length of the original stator blade trailing edges. With this design, the rotor blade stagger angle is fixed, but the stator stagger is variable through the variable geometry mechanisms on the J-79 compressor casing. Geometric characteristics of the rotor blades and stator vanes are listed in Table 1.

The rotor is driven by a hydraulic motor mounted inside the hub. An external hydraulic system, powered by a 50-horsepower electric motor is used to provide power to the hydraulic motor. With this system, rotor speed is continually variable from 0 rpm up to its maximum speed. Maximum speed in these tests was limited to 1300 rpm by overload constraints on the torque meter inserted between the hydraulic motor and the rotor drive shaft. The torque meter is a Himmelstein Model MCRT 9-02T(5-2) with a full-scale range of 424-inch pounds. The radial extent of the drive system and torque meter was kept small enough that the hub diameter could be kept constant at 12.8 inches throughout the test section and downstream ducting.

For some of the tests, a circumferential distortion screen was mounted upstream of the rotor. The screen is designed to provide a square wave distortion pattern with a circumferential extent of 180 degrees. It is fabricated from a perforated steel plate with an open area ratio of 60 percent. Previous calibrations (Ref. 7) of screens made from this material have shown that it provides a square-wave total pressure drop with a magnitude of approximately 1.1 times the dynamic pressure in the approaching flow. The mounting system for the distortion screen allows it to be indexed to different circumferential locations.

TABLE 1

GEOMETRIC CHARACTERISTICS OF ROTOR BLADES AND STATOR VANES

a. Rotor Blades

Blade Length		8.23 inches
Blade Chord		2.23 inches
Number of Blades		21
Stagger Angle; (Chord Angle) (from Axial)	Hub (r = 6.4") Mean Radius (r = 11.32") Tip (r = 14.63")	6.7 deg. 36.2 deg. 50.1 deg.
Camber Angle;	Hub Mean Radius Tip	28.7 deg. 21.5 deg. 14.5 deg.
Max. Thickness/Chord;	Hub Mean Radius Tip	0.130 0.070 0.039

b. Stator Vanes

Vane Length		8.31 inches
Vane Chord;	Hub Tip	1.62 inches 1.74 inches
Number of Vanes		28
Stagger Angle		Variable
Relative Twist (Positive Twist Increases Stagger)	Hub (r = 6.4") Mean Radius (r = 11.32") Tip (r = 14.71")	0 deg. 6.9 deg. 8.7 deg.
Max. Thickness/Chord;	Hub Tip	0.064 0.158

b. Instrumentation

The outer casing of the annular cascade test section has been modified to allow radial traverses with hot-film and total pressure probes far upstream of the rotor and immediately downstream of the rotor. The downstream station is located circumferentially half-way between two stator vanes and the probe sensing tips (pressure and hot-film) fall approximately at the axial location of the stator vane $1/4$ chord. The far upstream station is approximately 32 inches upstream of the rotor. In all of the experiments, the mass flow through the test section was determined by measuring the dynamic pressure in the constant area annulus at the far upstream station.

The total pressure measurements were made with a multi-tube rake which covers only a fraction (1.5 inches) of the total radial span (8.31 inches) of the annular cascade test section. The full span was covered by traversing the rake to different radial locations. Traversing the radius with a short rake allowed the rake to be aligned approximately with the local flow direction which was determined at each radial location from a Conrad arrowhead style yawmeter incorporated on the rake. Proceeding in this manner was time consuming but necessary since the radial variation in flow direction was very large in some tests, exceeding 30 degrees. Pressures detected by the rake were photographically recorded from a multitube manometer and analyzed later.

The three-dimensional velocity field upstream and downstream of the rotor was measured with a three-sensor hot-film anemometer system (triple probe system). A substantial portion of time was required to calibrate the triple probe system and develop data analysis techniques for obtaining three-component velocity data from the three anemometer voltage outputs. Although the triple-probe system had been calibrated previously for another program, preliminary calibration tests in this program indicated that the calibration was valid only over a small range of flow angles with respect to the probe axis of symmetry. Extending the calibration to be valid over a larger range of angles required that the equations relating the flow velocity components to the anemometer voltage outputs contain terms which account for flow interference between the hot-film sensors and the needles which support them. Inclusion of these interference terms results in a set of algebraic equations which are nonlinear and

coupled. An iteration process was used to solve these equations on-line using a Hewlett-Packard desk-top computer (HP-9825A). An on-line program was developed for the computer which used a large number of instantaneous anemometer voltage samples to determine the time averaged values of the three velocity components, the time-average of the velocity component cross products, and various statistical time averages of the fluctuating components. A detailed discussion of the triple-probe calibration and data analysis techniques is presented in Appendix A.

The output from the torquemeter was integrated for 10 seconds on an integrating voltmeter and the average of five such integrated readings was used to determine a single torque data point. This procedure was used to average out small random fluctuations which occur because the operating conditions are not absolutely steady. In addition to torque, the torquemeter provided an output of 60 pulses for each rotor revolution. This output was read on an electronic counter set to a one-second gate time to provide a direct rpm readout.

In preliminary tests, the presence of rotating stall was detected by a pressure transducer connected to a static pressure tap on the outer casing at the axial location of the rotor $1/4$ chord. However, it was found that a clearer indication of rotating stall was obtained from a total pressure probe mounted just upstream of the rotor. This method was used for the main body of the test program. In addition, rotating stall was evident in oscilloscope traces from the triple probe anemometer outputs. This indication of rotating stall was in agreement with the total pressure probe indicator.

c. Determination of Bearing Tare Torque

The rotor blades in the current configuration of the annular cascade are mounted on the first stage rotor disk from the J-79 and are not removable after assembly. The fixed nature of the rotor blade assembly created a problem in determining the tare torque generated by the bearings in the rotor drive system. Bearing torque values are required so that the aerodynamically generated torque on the rotor can be determined from overall torque measurements which include the bearing torque.

The value of the bearing tare torque as a function of rotor speed was determined by sealing the rotor in a small cavity between two annular disks. The configuration is sketched in the upper portion of Fig. 2. With the rotor sealed in this fashion, the torque required to drive the rotor consists of the bearing torque and the torque generated by aerodynamic forces due to the recirculating flow in the sealed cavity. The bearing torque will vary linearly with rotor speed (Ref. 8), while the aerodynamic torque will vary with the rotor speed raised to a power between $9/5$ and 2. The $9/5$ power will dominate if turbulent boundary layer friction is the primary aerodynamic mechanism (Ref. 9), while the power 2 will dominate if pressure drag is the primary mechanism.

Figure 2 show three sets of torque data taken on separate days. Each data set was fitted with two curves using the method of least squares. One curve assumed a $9/5$ power law for the aerodynamic losses and the other assumed a square power law. The square power law provided a slightly better fit to the data based on the sum of the squared errors. It is these curves which are shown in Fig. 2 fitted to the total torque data. The linear portions of the least square fits to the three sets of data are also shown in Fig. 2, labelled bearing torque. As can be seen, the three bearing torque estimates are reasonably consistent. The maximum difference between the three curves is less than 1.5 inch pounds and this maximum difference occurs at high rpm where the rotor torque during the experiments is high, minimizing the percentage error in the bearing torque estimate relative to the overall torque. The average of the three bearing torque curves was used as an estimate of the bearing torque for analysis of the data taken during the experimental program.

3. ISOLATED ROTOR

a. Inlet Flow Calibration

In preliminary tests, the annular cascade contained a hub section upstream of the rotor which was 30 inches shorter than that sketched in Fig. 1. During the preliminary tests, it was noted that the boundary layer on the hub upstream of the rotor separated intermittently on a fairly regular basis. The intermittent separation was independent of rotor speed; it occurred even with the

rotor stationary. Further investigation suggested that the separation was caused by a local unfavorable pressure gradient near the joint between the bullet nose and the constant diameter hub. Thus it was decided to modify the hub region near the inlet bell. A 30-inch hub extension was fabricated to move the bullet nose forward inside the large outer casing inlet bell (Fig. 1), where there is a favorable axial pressure gradient imposed by the inlet bell. Subsequent measurements with a pressure transducer connected to the total pressure survey rake showed that the separation was eliminated by the hub extension. Following this, radial surveys were performed to establish the uniformity of the total pressure in the constant area annulus far upstream of the rotor. The results are shown in Fig. 3.

In Fig. 3, the inlet total pressure coefficient, C_{PT_0} , is shown as a function of radius. The inlet total pressure coefficient is

$$C_{PT_0} = \frac{P_T - P_{T_0}}{\frac{1}{2} \rho U_0^2}$$

where P_T = Total pressure measured by the rake
 P_{T_0} = Total pressure measured by a fixed reference probe near mid-annulus far upstream of the rotor
 U_0 = Mean axial velocity far upstream
 ρ = Air density

Fig. 3 shows that the inlet flow to the annular cascade test section is quite uniform in total pressure except for the boundary layers on the hub and tip casings. Both boundary layers are thin; the hub boundary layer has a depth of approximately 0.1 inch and the tip boundary layer a depth of approximately 0.25 inch. These depths are negligible fractions of the radial span of the annular cascade test section.

Radial surveys of inlet flow velocity field taken with the hot-film triple probe at the same location as the total pressure data are shown in Fig. 4. These surveys were made at three different rotor speeds (500, 900 and 1200 rpm), with the mean axial velocity, U_0 , held constant at approximately 52.5 feet per second. At this value of U_0 , rotating stall inception occurs

on the rotor at approximately 1000 rpm. Thus the velocity surveys provide data for conditions well below stall inception (500 rpm), near stall inception (900 rpm), and after a steady state rotating stall has developed (1200 rpm).

Each part of Fig. 4 (a, b and c) presents results at a different rotor speed. The mean axial, \bar{U} , circumferential, \bar{V} , and radial, \bar{W} , velocity components are shown in each part along with the r.m.s. values (u' , v' , w') of the fluctuations in each velocity component. All the velocity data have been nondimensionalized by the mean inlet velocity, U_0 . The latter is calculated from the pressure difference between a total pressure probe in the cascade annulus and a static pressure tap on the outer casing, both at the upstream axial location of the radial velocity surveys.

Comparing parts a, b and c of Fig. 4 shows that the flow far upstream of the rotor is independent of rotor speed and of the presence or absence of rotating stall; all three parts provide results which are indistinguishable within the accuracy of the measurements. As expected from previous total pressure surveys at this location (Fig. 3), the dimensionless mean axial component has a nearly constant value ($\bar{U}/U_0 \approx 1$) with radius, and the circumferential and radial components are small. The circumferential component, \bar{V}/U_0 , does appear to contain a consistent trend with radius being positive near the hub and very slightly negative near the tip. The rms values of the circumferential, v'/U_0 , and radial, w'/U_0 , components lie in the range between 3 and 6 percent while the rms of the axial component, u'/U_0 , is smaller ($u'/U_0 \approx 1$ percent). While rms values of 3 to 6 percent for the circumferential and radial fluctuations are relatively large by wind tunnel standards, they are not surprising for the inlet region of a low hub-to-tip ratio annular cascade.

In summary, the inlet total pressure and velocity surveys provide results which appear to be satisfactory as undistorted inlet conditions for the rotor. Moreover, since the data behave as expected, it indicates that the triple probe anemometer system and on-line computer program for data analysis operated properly.

b. Velocity Field Downstream of Isolated Rotor

Radial surveys were performed with the triple probe downstream of the rotor with the probe shaft at the axial location of the mid-chord of the stator row when installed. This places the sensing elements on the triple probe approximately 1 inch downstream of the rotor blade trailing edges. The radial surveys were performed at 13 different rotor speeds, covering flow conditions from well below rotating stall inception to well above inception. The major results of the surveys are presented in Figs. 5 and 6. Mean velocity components are shown in Fig. 5, and the rms of the fluctuations are shown in Fig. 6. Numerical values of the above data and of some other parameters are tabulated in the computer printouts of Appendix B.

Each part, a through i of Fig. 5, presents mean velocity data for a different rotor speed. In addition, parts c and g present data from repeat runs made on different days and at different ambient temperatures. The date, air temperature and mean inlet velocity, U_0 , are given in a box for each run and the absence or presence of rotating stall is noted below the box. The repeat run made at 800 rpm (Fig. 9c), which is below stall inception agrees quite well with the original survey. The repeat run after stall inception (Fig. 9g), 1050 rpm, shows somewhat more scatter but the agreement between surveys is still satisfactory.

At low rotor speeds, the mean axial velocity, \bar{U} is approximately constant in the central portion of the annulus and decreases near the hub and tip regions. As rotor speed increases towards rotating stall inception, the \bar{U} distribution changes shape, displaying maxima at radial locations near the hub and near the tip and a minimum near mid-annulus. As rotating stall develops (rpm \gtrsim 1000), the maximum near the tip disappears and \bar{U} begins to decrease with increasing radius. Once steady rotating stall has developed (rpm \gtrsim 1100), the decrease in \bar{U} with increasing radius becomes large. Earlier tests with a traversing total pressure probe had shown that rotating stall on this rotor covered approximately the outermost 70 percent of the blade span, with the remaining region being apparently free of rotating stall. Visual observation of the signals from the hot-film sensors suggested the same behavior. Thus the

large decrease in \bar{U} with increasing radius once steady rotating stall has formed is not surprising since the axial velocity in the stall cells is small. Apparently the deficit in mean axial velocity in the stalled regions forces more of the flow to pass through the unstalled hub region on this low hub-to-tip ratio rotor. The increased axial velocity near the hub tends to stabilize this region and prevent rotating stall from becoming full span as the rotor speed is increased.

Consider now the mean circumferential velocity component \bar{V} in Fig. 5. There are two trends in \bar{V} with increasing rotor speed. First the overall magnitude of \bar{V} increases with rotor speed as expected. Second the shape of the radial distribution changes with rotor speed. At low rotor speeds, \bar{V} is a maximum near the hub and decreases towards the tip. This is a result of the twist in the rotor blades; at low rotor speeds the blades have more twist than that required to account for the increase in circumferential blade velocity with radius. As rotor speed is increased in the unstalled region, the decrease in \bar{V} with radius becomes progressively less pronounced, as expected. However, the \bar{V} distribution near the blade tip region is unusual. At rotor speeds of 800 rpm and above, there is a region near the tip in which \bar{V} increases very rapidly with radius. At rotor speeds of 800 and 900 rpm, the region of rapidly increasing \bar{V} occurs at $\Delta r \approx 7.3$ inches and corresponds to the region in which \bar{U} is decreasing rapidly. Rotating stall was not detected at these rotor speeds, so the unusual behavior of \bar{V} near the tip may be a result of secondary flow phenomena near the tip. On the other hand, the \bar{V} behavior may be evidence of a small undetected rotating stall confined to the blade tip region.

For rotor speeds at which rotating stall was detected ($\gtrsim 950$ rpm), the region of rapidly increasing \bar{V} begins to extend further into the annulus as rotor speed increases. At the maximum rotor speed tested (1300 rpm), \bar{V} begins to increase at $\Delta r \approx 5$ inches while \bar{U} begins its most rapid decrease with radius at this same radius. The increase in \bar{V} in the presence of rotating stall is consistent with the description of flow in a rotating stall cell presented in Ref. 10. There it was found that very high circumferential velocities

and low axial velocities exist in a stall cell immediately upstream of the first rotor in a two-stage compressor in part span rotating stall. Immediately downstream of the same rotor, although the absolute magnitude of the velocity decreased, the flow in the cell was still predominantly circumferential. Moreover, this circumferential velocity increased with increasing radius. Thus one would expect the mean circumferential velocity, which is an integral of the velocity in the cell and external to the cell, to show the behavior displayed by the current data in the presence of rotating stall.

The final component of velocity presented in Fig. 5 is the mean radial velocity, \bar{W} . At low rotor speeds, this component is small and consistently negative over most of the radius. As rotor speed is increased, \bar{W} approaches zero and becomes more irregular with radius. The scatter of about zero is probably within the accuracy of the triple probe measurements. Once steady rotating stall is established (rpm \gtrsim 1100), \bar{W} appears to take a small consistently positive value in the outer portion of the annulus. However, it is not certain that the \bar{W} data are reliable in this region of large velocity fluctuations. The \bar{U} and \bar{V} components are probably more reliable because the effect of velocity fluctuations in these components is made less severe by adjusting the pointer angle on the probe as discussed in Appendix A.

The rms of the fluctuations in the velocity components are presented in Fig. 6. At the three lowest rotor speeds (400, 500 and 600 rpm), the rms components are all approximately constant at 3 to 5 percent of U_0 except for small increases near the hub and tip. At rotor speeds above 600 rpm, the rms values begin to increase with increasing rotor speed except for the region close to the hub. The increase is gradual and appears to affect all three components equally until rotating stall occurs. Once rotating stall is present, all components continue to increase with rotor speed, but the rms axial component, u' , increases more rapidly. At rotor speeds above 1000 rpm, the u' component is distinctly larger than v' and w' , except perhaps in the region close to the hub. The larger values of u' are most likely caused by the combination of low axial flow velocity within the stall cell and larger axial flow velocity in the free stream region between cells. This difference apparently is larger than the difference in circumferential velocities within the cell and external to the cell.

c. Integrated Velocity Components and Comparisons With Other Measurements

The velocity data presented above illustrate that the time averaged velocity components downstream of the rotor in the annular cascade are very nonuniform with radius and that the fluctuations in the instantaneous values become large even before rotating stall inception occurs. The complexity of both the flow field and the on-line computer program for analysis of the triple-probe data raise questions regarding the accuracy of the results. Thus it is of interest to assess the accuracy of the data through comparisons with results from measurements performed with other instrumentation or through comparisons in which the correct results are known. Three such comparisons are presented in the following paragraphs.

The first comparison is concerned with the swirl angle, β_2 , downstream of the rotor. Total pressure data which will be presented shortly were measured with a multi-tube rake which covers only a fraction (1.5 inches) of the total radial span (8.31 inches) of the annular cascade test section. The full span was covered by traversing the rake to different radial locations. The total pressure rake contained a Conrad arrowhead style yawmeter at its radial center which was used to align the rake with the local flow direction at this center. The flow angle determined by this alignment procedure was recorded for each rake position and rotor speed. Since four radial positions of the rake were used in each total pressure survey, the swirl angles downstream of the rotor at these four locations are available for comparison with swirl angles calculated from the triple-probe mean velocity components.

The swirl angle calculated from the velocity data is given by

$$\beta_2 = \tan^{-1} \left(\frac{\bar{V}}{\bar{U}} \right)$$

at the radial location of the yawmeter measurements. The velocity data were not measured at exactly the radial locations corresponding to the yawmeter measurements, so each component \bar{U} and \bar{V} of the velocity data were assumed to vary linearly between the two points closest to the yawmeter radial location. Swirl angles calculated in this way from the velocity measurements are compared with the yawmeter results in Fig. 7.

Fig. 7 presents swirl angle comparisons as a function of rotor speed for each of the four radial locations at which yawmeter data are available. As can be seen the agreement between yawmeter and triple probe results is excellent except for one point at a rotor speed of 1300 rpm and $\Delta r = 5.41$ inches (Fig. 7(b)). In view of the excellent agreement everywhere else, it is probable that the yawmeter angle was misread by an increment of 5 degrees for this point. Such an error is easy to make when concentration is focussed on interpolating between the smallest angular divisions (1 deg) on the protractor used to read yawmeter angle.

The excellent agreement between swirl angles determined from the yawmeter and from the triple probe indicates that the ratio between the mean circumferential and axial velocity components, \bar{V}/\bar{U} , is determined with satisfactory accuracy by the triple probe data system. Moreover, the accuracy is maintained everywhere in the flow field and also in the presence of rotating stall (rpm $\gtrsim 1000$).

A second assessment of the accuracy of the triple probe data is afforded by application of the flow continuity equation. This requires that the area weighted integral of the mean axial velocity component, \bar{U} , be constant at all locations in the flow field, or on a dimensionless basis

$$\frac{1}{S} \int_S \frac{\bar{U}}{\bar{U}_0} dS = 1$$

where S is the annulus area. The radial distribution of, \bar{U}/\bar{U}_0 , upstream and downstream of the rotor have been integrated as indicated above and the results are presented in Fig. 8. As expected, integration of the radial profiles at the inlet (Fig. 4) provide the desired results to within better than 1 percent. Integration of the downstream profiles (Fig. 5) provide results which are excellent at the lowest rotor speeds but which become progressively lower as rotor speed is increased until they are 5 percent low just prior to the occurrence of relatively steady rotating stall (rpm > 1000). After this speed there is a small but sudden increase in the integral to nearly its correct value and then a slow increase with rotor speed. The final value of the integral at 1300 rpm is about 4 percent high. In general, the trends with rotor speed displayed

by the downstream integrals are small but consistent. The reasons for this behavior are unknown. However, the overall accuracy of the integrals is within 5 percent of the correct value over the complete rotor speed range of the tests. While higher accuracy would be desirable, the apparent accuracy is considered acceptable in view of the nonuniformity and unsteadiness of the flow field being measured.

The final comparison to be made is based on a relation between the torque required to drive the rotor and the flow field downstream of the rotor. In Ref. 11, it is shown that the overall torque on an isolated rotor depends only on the overall change on angular momentum through the blade row. This same result was reached independently during the current study (Ref. 12). For a constant area annulus in incompressible flow with undistorted axial inflow upstream of the rotor, the relation between the rotor torque and the downstream flow field is

$$\tau = \int_S \rho U V r dS \quad (1)$$

where

- r = radius
- S = annulus cross-sectional area
- τ = rotor torque
- U = axial velocity downstream of the rotor
- V = circumferential velocity downstream of the rotor in duct-fixed coordinates

The above relation applies to the annular cascade configuration used in the current experiments.

Now define a torque coefficient, C_τ , as

$$C_\tau \equiv \frac{2\omega\tau}{\rho U_o^3 S}$$

where ω is the rotor angular velocity. Then using Eq. (1), the relation between C_τ and the downstream flow field is

$$C_T \equiv \frac{2\omega T}{\rho U_o^3 S} = \frac{1}{S} \int_S \frac{2r\omega}{U_o} \frac{\overline{UV}}{U_o^2} ds \quad (2)$$

where $(\overline{\quad})$ indicates a time average of the instantaneous velocity product. The time average is required because the instantaneous flow field is unsteady due to rotor wake passage in the duct fixed coordinate system. (The time average is assumed to be equivalent to a circumferential average in a frame of reference which rotates with the blades.)

The value of C_T can be calculated from the measured values of the torque, T , required to drive the rotor and, independently, it can be calculated by integration of \overline{UV} as indicated by Eq. (2). The local values of \overline{UV} determined by the triple-probe surveys are tabulated in Appendix B along with the area integral of Eq. (2). The results for the isolated rotor are shown in Fig. 9.

Fig. 9 presents comparisons of the torque coefficients over the complete speed range (400 to 1300 rpm) of the tests. The state of the observed rotating stalls is noted as a function of rotor speed in the lower portion of Fig. 9. It is evident that the two independent means of obtaining C_T provide results which are essentially identical at rotor speeds of 1000 rpm or less. In this speed range, rotating stall is either nonexistent or else occurs only occasionally. Once rotating stall is present on a frequent or steady basis, the values of C_T calculated from the velocity data become 10 to 12 percent larger than those calculated from the torque data.

The excellent agreement between the torque coefficients derived from torque measurements and from velocity measurements in the absence of steady-state rotating stall provides confidence in the accuracy of both sets of measurements in this flow region. Once rotating stall has developed, the torque measurements provide the most reliable data because the triple probe velocity data may be influenced by instantaneous excursions in flow angle which are beyond the range of validity of the calibration and data analysis procedure. The apparent deterioration in accuracy in calculating C_T from triple probe data in

the presence of steady rotating stall does not compromise the experimental program on rotor-stator interaction effects; the principal data required for this study are obtained from the torque-meter data and total pressure measurements. The triple probe is used only to provide the radial distributions of mean axial flow for mass flow averaging of the total pressure data. The continuity integrals in Fig. 8 indicate that these data are accurate to within 5 percent at all flow conditions.

d. Rotor Torque, Total Pressure Rise, and Loss Coefficients

As noted in Section II-A, application of the existing rotating stall stability theory requires an input the relative losses across the rotor in a blade-fixed coordinate system. In previous studies of a high hub-to-tip ratio rotor (Refs. 3 and 7), the area averaged relative loss coefficient, $\Delta \bar{C}_{P_{TR}}$, was taken as the difference between an area averaged work coefficient, \bar{C}_W , and the area averaged total pressure rise across the rotor, $\Delta \bar{C}_{P_T}$. That is,

$$\Delta \bar{C}_{P_{TR}} = \bar{C}_W - \Delta \bar{C}_{P_T} \quad (3)$$

where

$$\bar{C}_W = \frac{1}{S} \int_S \frac{2r\omega}{U_0} \frac{\bar{V}}{U_0} ds \quad (4)$$

$$\Delta \bar{C}_{P_T} = \frac{1}{S} \int_S \frac{P_{T_2} - P_{T_0}}{\frac{1}{2} \rho U_0^2} ds \quad (5)$$

Note that the torque coefficient in Eq. (2) and the work coefficient in Eq. (4) differ in that the torque coefficient contains \overline{UV}/U_0^2 in the integral while the work coefficient contains only \bar{V}/U_0 . If the flow is completely steady in duct-fixed coordinates, $\overline{UV}/U_0^2 = (\bar{U}/U_0)(\bar{V}/U_0)^*$ and the difference between the torque and

* This approximation is quite accurate for the data obtained in the absence of rotating stall. In reality, $\overline{UV}/U_0^2 - (\bar{U}/U_0)(\bar{V}/U_0) = \overline{u'v'}/U_0^2$. The values of $\overline{u'v'}/U_0^2$ are listed in Appendix B (labeled uv') for each data point. Inspection of the tables shows that uv' is negligible in magnitude except for rotor speeds above 1000 rpm where frequent to steady rotating stall was present on the isolated rotor.

work coefficients is that the torque coefficient is a mass flow averaged value of the local work coefficient. It follows that the determination of an average relative loss coefficient from the torque data and total pressure data requires mass flow averaging of the total pressure data.

The actual expression relating the mass flow averaged relative loss coefficient to the torque and total pressure data can be obtained by noting that in a rotating frame of reference, the quantity conserved in loss-free flow, (Ref. 12), is

$$P_{TR} = p + \frac{1}{2}\rho(U^2 + W^2 + V_R^2) - \rho\omega^2 r^2 \quad (6)$$

where

p = static pressure
 (U, W, V_R) = axial, radial and circumferential velocity components in relative (blade fixed) coordinate system.

Note that P_{TR} differs from the usual definition of relative total pressure by the last term on the right in Eq. (6). The loss in total pressure due to viscosity along the streamline as it passes through the rotor will be $(P_{TR_0} - P_{TR_2})$ where subscripts 0 and 2 indicate stations upstream and downstream of the rotor. The mass flow average of these relative losses in a constant area annulus is

$$\widetilde{\Delta P_{TR}} = \frac{1}{U_0 S} \int_S [(UP_{TR})_0 - (UP_{TR})_2] ds \quad (7)$$

Using Eqs. (4), (5) and (6) and specifying uniform inflow, $(U)_0 = U_0$ and

P_{TR_0} = constant, one can show that the mass flow averaged relative loss coefficient, $\widetilde{\Delta C_{P_{TR}}} (= \widetilde{\Delta P_{TR}} / \frac{1}{2}\rho U_0^2)$ is given by

$$\widetilde{\Delta C_{P_{TR}}} = \frac{1}{S} \int_S \left[\left(\frac{2\omega r}{U_0} \frac{\bar{U}V}{U_0^2} \right) - \left(\frac{\bar{U}}{U_0} \Delta C_{P_T} \right) \right] ds = C_T - \widetilde{\Delta C_{P_T}} \quad (8)$$

where

$$\widetilde{\Delta C_{P_T}} = \frac{1}{S} \int_S \frac{\bar{U}}{U_0} \Delta C_{P_T} ds \quad (9)$$

In view of Eq. (8), the difference between the torque coefficient C_T and the area averaged pressure rise coefficient, $\Delta \overline{C_{P_T}}$ (Eq. (5)), represents the relative loss across the rotor only if the axial velocity downstream of the rotor is a constant with radius. The axial velocity profiles presented in Fig. 5 show that this is not the case. Thus it is of interest to compare the results from mass flow and area averaging of the total pressures to determine the magnitude of the difference between the two procedures. This comparison will be presented shortly.

Radial distributions of the local value of the torque coefficient $(2\omega r/U_0)(\overline{U}/U_0^2)$ and mass flow weighted total pressure rise coefficient, $(\overline{U}/U_0)\Delta C_{P_T}$, are presented in Fig. 10 for the isolated rotor. The data used in Fig. 10 were all obtained with the mean axial velocity, U_0 , far upstream of the rotor held constant at approximately 53 feet per second. Each part, a through i, of Fig. 10 presents data at different rotor speeds. In the rotor speed range between 700 and 1000, the total pressures were not completely steady so multiple total pressure surveys were made to define the extremes. In addition to the multiple total pressure surveys, two of the triple probe velocity surveys were repeated on different days with different ambient temperatures. Both sets of local torque coefficient, are shown for these repeated surveys (Figs. 10c and 10f).

As indicated by Eq. (8), the difference between the radial distribution of $\frac{2\omega r}{U_0} \frac{\overline{U}}{U_0^2}$ and $\frac{\overline{U}}{U_0} \Delta C_{P_T}$ gives the radial distribution of the rotor's mass-flow weighted relative loss coefficient (as measured at an axial location approximately 1 inch downstream of the rotor blade trailing edges). At the lowest rotor speeds (400 to 600 RPM), the majority of the losses across the rotor occur near the hub and tip regions. At 700 RPM, the rotor begins to incur significant losses over the complete span. As rotor speed is increased further, the losses increase in magnitude with increasing rotor speed except in a small region near the hub where they appear to remain relatively constant up to a rotor speed of approximately 1050 to 1100 RPM. As noted on the separate parts of Fig. 10, first indication of the presence of rotating stall occurred at a rotor speed of 950 RPM, and it becomes steady rotating stall at 1100 RPM. The

data presented in Fig. 10 show that the rotor losses on the outer three-quarters of its span begin to increase rapidly at rotor speeds well below those at which rotating stall was detected and that the hub region incurs low losses even after rotating stall has started. In fact, it is not possible to deduce the presence of rotating stall from inspection of these data.

The radial distributions of the mass flow weighted total pressure rise, $(\bar{u}/u_0)\Delta C_{P_T}$, have been integrated over the annulus area to obtain the mass flow averaged total pressure rise $\tilde{\Delta C_{P_T}}$. These data are presented in Fig. 11. At rotor speeds where multiple radial surveys were measured, each distribution was integrated and the average of these integrals is shown in Fig. 11. The values of $\tilde{\Delta C_{P_T}}$ have been corrected to eliminate small inaccuracies in the axial velocity component derived from the triple probe data. The correction was made as follows:

$$\tilde{\Delta C_{P_T}} = \frac{\frac{1}{S} \int_S \frac{\bar{u}}{u_0} \Delta C_{P_T} ds}{\frac{1}{S} \int_S \frac{\bar{u}}{u_0} ds} \quad (10)$$

where $\frac{1}{S} \int_S \frac{\bar{u}}{u_0} ds \approx 1$. The latter integral was evaluated and presented in Fig. 8 for all of the velocity surveys on the isolated rotor. Its value was within 5 percent of unity for all cases tested. Also shown in Fig. 11 is the torque coefficient, C_T , derived from the torquemeter data.

The difference between C_T and $\tilde{\Delta C_{P_T}}$ is the mass flow averaged relative loss coefficient $\tilde{\Delta C_{P_{TR}}}$ for the rotor (Eq. (8)). This relative loss coefficient is the third variable in Fig. 11.

It was pointed out earlier that in past studies on a high hub-to-tip ratio rotor, the relative loss coefficient across the rotor was taken as the difference between an area-averaged work coefficient, \bar{C}_W , and the area-averaged total pressure rise, $\bar{\Delta C_{P_T}}$, across the rotor (Eq. (3)). Both of these quantities lack the axial velocity ratio, \bar{u}/u_0 , which occurs in the mass flow average of Eq. (8)). In particular, it was noted that the difference between the torque coefficient, C_T , (which is a mass-flow averaged parameter)

and the area averaged total pressure rise coefficient, $\overline{\Delta C_{p_T}}$ (which is not mass-flow averaged) represents the relative losses across the rotor only if the axial flow velocity downstream of the rotor is constant with radius. The velocity data presented in Fig. 5 show that the axial velocity, \bar{U} , downstream of the rotor is far from being constant with radius. Thus, it was expected that there would be significant differences between $\widehat{\Delta C_{p_T}}$ and $\overline{\Delta C_{p_T}}$.

Since the determination of mass-flow averages requires the measurement of the axial velocity distribution, which is a difficult measurement, it is of interest to compare the results of mass-flow averaging with the results of area-averaging. This has been done in Fig. 11 where the total pressure and relative loss results are presented for both mass-flow and area averaging. It can be seen that the mass-flow and area averages agree extremely well except at rotor speeds of 1200 and 1300 RPM, where steady large-amplitude rotating stall was present during the measurements. In fact, the agreement is maintained at rotor speeds well above those at which rotating stall was first detected. The first indication of rotating stall is marked by an arrow in Fig. 11. The reason for the agreement between the mass-flow averaged and area averaged total pressure rise across the rotor is unknown at present. However, if such agreement can be assumed to hold in general, then the determination of rotor losses becomes a much simpler experimental task, requiring only torque and total pressure measurements. Further evidence of this phenomenon will be presented in the rotor-stator stage data.

The data presented in Fig. 11 are sufficient to use as inputs to the existing rotating stall stability theory to investigate the ability of the theory to predict rotating stall inception on a low hub-to-tip ratio rotor. This has been done and the results are presented in a later subsection.

4. ROTOR-STATOR STAGE

a. Rotor Torque

As noted in Section II-A, previous studies on a high hub-to-tip rotor configuration of the annular cascade showed that the addition of a closely coupled stator row downstream of a rotor caused the rotor to generate a significantly higher total pressure rise than that generated by the isolated rotor with the same inlet conditions. The reason for this higher total pressure rise was not determined, but it was speculated that it could be caused by a larger work input from the rotor in the stage or a reduction in the losses across the rotor. In the present program resolution of these possibilities was approached through measurement of the torque input to a rotor in isolation and to the same rotor in a rotor-stator stage. In this case, the annular cascade has a much lower hub-to-tip ratio (0.44) than that used previously, so it is of interest to see if the rotor-stator interference effects are still in evidence as well as to determine if the rotor torque depends on the presence of a downstream stator row.

The results of the torque measurements on the rotor in the stage are compared to those measured on the isolated rotor in Fig. 12. These data were obtained with constant mean axial velocity ($U_o \approx 53$ ft/sec) in the annulus far upstream of the rotor. Data for the rotor in the stage are shown for three different stator stagger angles, δ_s , at the mean radius of the annular cascade. The middle stagger angle, 22.9 deg., corresponds approximately to the original design operating condition for the first stage of the J-79 compressor from which this low speed stage was adopted.

As can be seen in Fig. 12, there is a small but distinct increase in rotor torque when the stator row is added downstream of the rotor. Surprisingly, at rotor speeds up to approximately 800 RPM, the increase in rotor torque is largest for the stators with the lowest loading ($\delta_s = 32.9$ deg.) and smallest for the highest loading ($\delta_s = 12.9$ deg.). Above 800 RPM, there is no consistent trend between torque and stator stagger angle; but the staged-rotor torque remains above that measured on the isolated rotor. Thus it would

appear that the addition of a stator row downstream of this low hub-to-tip ratio rotor increases the torque required to drive the rotor even though upstream flow conditions are held constant. It remains to be seen whether the total pressure rise across this rotor is affected by the presence of the stator row in a fashion similar to that observed on the high hub-to-tip ratio rotor and rotor-stator stage. The results of the total pressure surveys are presented below.

b. Total Pressure Distribution on Rotor

Following the rotor torque measurements, radial distributions of total pressure between the rotor and stator were measured for a variety of rotor speeds, again with the mean axial velocity, U_o , held constant at approximately 53 ft/sec. In all, surveys were made for the same 13 rotor speeds as were tested with the isolated rotor, and for three different stagger angle settings of the stator row. As with the isolated rotor, it was found that the total pressures were not entirely steady in time, particularly in the mid-range of rotor speeds. Thus, two sets of total pressure data were taken for each test to define the extremes. The results of these measurements are compared to the equivalent measurements on the isolated rotor in Figs. 13 and 14. Fig. 13 presents the results for a stator stagger, δ_s , angle of 12.9 deg. and Fig. 14 presents those obtained with $\delta_s = 32.9$ deg. Similar data are available for $\delta_s = 22.9$ deg. but are not presented herein since the two sets of data shown are sufficient to illustrate trends.

The different parts, a through i, of Figs. 13 and 14 present data for different rotor speeds. The data obtained on the isolated rotor are shown as dashed lines while that obtained on the rotor in the stage are shown as symbols. The presence or absence of rotating stall is noted on each figure. On the isolated rotor, rotating stall was first detected at a rotor speed of approximately 950 RPM. With the stators installed, rotating stall inception was delayed to higher rotor speeds, approximately 1050 RPM for $\delta_s = 12.9$ deg. and 1100 RPM for $\delta_s = 32.9$ deg. These delays are similar to those observed on the high hub-to-tip ratio stage tested previously.

For the smallest stator stagger angle (Fig. 13, $\delta_s = 12.9$ deg.), the total pressure rise across the isolated rotor and across the rotor in the stage are similar at low rotor speeds. As rotor speed is increased, the rotor in the stage displays progressively more total pressure rise than the isolated rotor in the lower portion of the annulus. In fact, the staged rotor begins to develop a peak in total pressure rise at a distance of approximately 2-1/2 inches from the hub for rotor speeds as low as 800 RPM. This peak grows as rotor speed is increased further. Very close to the tip, the isolated rotor and staged rotor display similar total pressure behavior even after the isolated rotor has entered rotating stall (950 RPM). This similarity is maintained until the staged rotor enters rotating stall (1050 RPM). Once the staged rotor enters rotating stall, the tip total pressures drop suddenly while the remainder of the annulus still displays a substantial increase in total pressure for the staged rotor. As rotor speed is increased further, the deficit in total pressure near the tip of the staged rotor moves progressively farther down into the annulus.

At the higher stator stagger angle (Fig. 14, $\delta_s = 32.9$ deg.), the general trends observed with $\delta_s = 12.9$ deg. remain unchanged but the magnitudes of the effects differ. The peak in total pressure on the staged rotor still develops but its magnitude is not as large and it occurs at a slightly smaller radius ($\Delta r \approx 2$ in.). Moreover, the sudden drop in total pressure near the tip is delayed from 1050 to 1100 RPM in correspondence with the delay in rotating stall inception on this stage.

In general the radial distributions of total pressure rise across the isolated rotor and staged rotor in this low hub-to-tip ratio configuration display trends similar to those observed on the high hub-to-tip ratio configuration (Ref. 3), that is the staged rotor generates a greater total pressure rise than the isolated rotor even before rotating stall inception. However, the increased total pressure on the current low hub-to-tip ratio configuration is much more nonuniform with radius than it was on the high hub-to-tip ratio unit. In any event, it would appear that both high and low hub-to-tip ratio rotors display interference effects when closely coupled to a downstream stator row.

c. Axial Velocity and Mass Flow Weighted Total Pressure
Rise Distributions

As discussed in Section II C.4, the determination of relative losses across the rotor requires knowledge of the rotor torque coefficient and the mass-flow averaged total pressure rise (Eq. 8)). The latter is determined through integration of the mass-flow weighted total pressure rise coefficient over the annulus area. Radial distributions of dimensionless mass-flow weighted total pressure rise coefficient $(\bar{U}/U_I) \Delta C_{P_T}$ are presented in Fig. 15 along with radial distributions of the dimensionless axial velocity, \bar{U}/U_I . In each case, the data are made dimensionless through division by U_I where

$$U_I = \frac{1}{S} \int_S \bar{U} ds \quad (11)$$

Division by U_I compensates for inaccuracies in measuring the axial flow component of velocity (see discussion surrounding Eq. (10)) and provides a consistent basis for comparing data from the isolated rotor with data measured mid-way between the stators at an axial location near the stator 1/4 chord. The presence of the stators accelerates the flow at the measuring location. Division of the data by U_I assumes that the mid-vane space radial surveys of axial velocity are typical of the distributions throughout the passage space between the stators. The flow acceleration induced by the stators does not affect the total pressure rise coefficient, ΔC_{P_T} , since the total pressure downstream of the rotor is conserved, unless the measuring location lies in a region of flow separation generated at the stator leading edges.

Fig. 15 compares data taken on the isolated rotor with data obtained on the rotor-stator stage. The stage data are presented for two different stator stagger angles. In all cases, the mean axial velocity, U_0 , was held constant at approximately 53 ft/sec and the rotor speed was varied. Each part (a through i) of Fig. 15 present data for a different rotor speed. When more than one radial survey was taken for a given condition, the plotted data are averages of the multiple survey results.

The dimensionless axial flow velocity profiles on the isolated rotor and the rotor in the stage are identical to within the experimental accuracy at the lower rotor speeds (up to 800 RPM). However, the mass flow weighted total pressure rise coefficients display increasingly larger differences as rotor speed is increased in this range. In general, the rotor in the stage displays an increase in mass-flow weighted total pressure rise over that observed with the isolated rotor. At a rotor speed of 900 RPM, the axial velocity profile for the state with a stagger angle $\delta_s = 32.9$ deg. remains essentially similar to that measured on the isolated rotor while the stage with $\delta_s = 12.9$ deg. displays a redistribution of the axial flow in the lower half of the annulus. At higher rotor speeds, the axial flow velocity is redistributed on the stage for both stator stagger angles. In the outer portion of the annulus, the results on the stage at both stagger angles are similar and both display higher axial velocities than the isolated rotor. In the lower portion of the annulus, the effect of the stators depends on stator stagger angle, but the results for both stagger angles show reduced axial velocities over those observed on the isolated rotor. At the highest rotor speeds (1200 and 1300 RPM) where steady rotating stall was present on all three configurations, the rotor in the stage displays significantly higher axial velocities near the tip than does the isolated rotor. In all cases above 800 RPM, the mass flow weighted total pressure rise distributions on the rotor in the stage are substantially different from those observed on the isolated rotor.

In general, the mass flow weighted total pressure rise data in Fig. 15 follows the trends displayed by the total pressure rise data presented previously. The specific shapes of the distributions are different because the axial flow velocity is not uniform with radius. However, the comparative differences between the isolated rotor and the rotor in the stage remain. The presence of the stator row causes a redistribution in the axial flow with radius at rotor speeds above 800 RPM but this effect is not nearly as large as the effect on total pressure, except perhaps near the rotor tip under conditions when steady rotating stall was present on all three configurations. The latter data are suspect because the large instantaneous velocity excursions during stall may be beyond the range of validity of the triple probe calibration.

d. Rotor Torque, Total Pressure Rise and Loss Coefficients

As with the isolated rotor, there are several integrated flow parameters of interest. These are the area-averaged values of axial flow velocity, total pressure rise coefficient, and mass-flow weighted total pressure rise coefficient. The integral of the velocity derived torque coefficient was also evaluated for the isolated rotor. However, for the rotor in the stage, this particular integral does not apply because the stator row provides an additional body force on the flow downstream of the rotor which makes the integral of the velocity field in Eq. (2) inapplicable. The area averaged axial flow velocity, total pressure rise coefficient and mass-flow weighted total pressure rise coefficient are presented in Figs. 16 and 17. Torque coefficients derived from the torquemeter data and integrated total pressure rise and relative loss coefficients are presented in Figs. 18, 19 and 20.

The area weighted integral of the dimensionless mean axial flow velocity, \bar{U}/U_0 is presented in Fig. 16 as a function of rotor speed for both the isolated rotor and the rotor in the stage. The isolated rotor data have been presented previously in Fig. 8. In the discussion of that figure it was noted that by flow continuity the value of the integral should be unity for this case. Deviations from unity are a measure of the accuracy of the triple probe data. The deviations ranged from -5 to +4 percent for this case, acceptable results considering the nonuniformity and unsteadiness of the flow field.

In the case of the stage, it was noted in Section II-D.3 that the axial flow at the measuring station is accelerated by the displacement effect of the stators. This effect is evident in the data for the stage where the integrated values are all greater than unity. However, a simple solid body displacement effect is not sufficient to explain the increases in the integral at low and high rotor speeds. This result is probably caused by additional displacement effects from boundary-layer separation on the stator vanes. At low rotor speeds, particularly for the larger stator stagger angle, $\delta_s = 32.9$ deg., the stators may have separated flow on the underside (pressure side) of the vanes. As rotor speed is increased the pressure side separation apparently

vanishes and is eventually replaced by flow separation on the suction surface. For the lower stator stagger angle, $\delta_s = 12.9$ deg., the suction side separation appears to occur well before rotating stall is detected. (The first indication of detectable rotating stall is denoted by arrows in Fig. 16.) For the larger stagger angle, the axial flow integral does not begin to increase until rotating stall occurs. In this case, the apparent increase in axial flow velocity is uncertain because the presence of rotating stall may cause errors in the triple probe data. The same comment applies to the data after rotating stall inception on the stage with $\delta_s = 12.9$ deg. However, in this case the increase in the integral begins well before stall inception and these data should be reliable. The fact that the largest deviations in the axial flow integral for the rotor in the stage are positive indicates that the probe location was not in a region of separated flow from the stators. Location in such a region should cause a decrease in the integral of Fig. 16.

In Section II-C.4 it was shown that mass flow averaging and area averaging of the rotor total pressure rise coefficient provide almost identical results for the isolated rotor in the absence of steady rotating stall (Fig. 11). A similar comparison of the data obtained with the rotor in the state has been made. The stage results are shown in Fig. 17 along with the isolated rotor results. Here the dimensionless mass-flow averaged total pressure rise integrals are plotted versus the area averaged total pressure rise integrals. Data taken during rotating stall are indicated by tails on the symbols. As with previous comparisons, the velocity data have been normalized through division by U_I to eliminate small inaccuracies in the triple probe data and flow acceleration effects caused by the presence of the stators.

The solid line in Fig. 17 represents the results which would be obtained if mass flow averaging and area averaging provide identical results. It is evident from the data that the two types of averaging provide essentially the same result in the absence of rotating stall. The unstalled mass flow averaged data are consistently very slightly larger than the area averaged data, but the difference is considered negligible. It may result from the fact that fewer spanwise data points were available for mass flow averaging. The spanwise velocity data were taken at 20 radial locations while the total pressure

data were taken at 28 radial locations, including locations closer to the hub and tip which could not be reached with the triple probe. Thus, the earlier discussion on the equivalence of mass flow averaging and area averaging of the total pressure appears to apply to the staged rotor as well as the isolated rotor in the absence of rotating stall. After stall inception, the results of mass-flow averaging of the total pressure rise coefficient differ from those of area averaging, but these apparent differences may be a result of inaccuracies in the triple probe velocity data for this situation.

As discussed previously, the rotor in a stage generates a larger total pressure rise and requires a larger driving torque than that found for an isolated rotor with the same upstream flow conditions. One of the aims of the current program is to determine if the rotor torque changes when a downstream stator row is added (it does), and another is to investigate the effect of rotor-stator interference on the losses across the rotor. In Section II-C4, the relation between relative losses, torque coefficient and mass-flow averaged total pressure rise was presented (Eq. (8)); the relative loss coefficient for rotor is simply the difference between the torque coefficient and the mass-flow averaged total pressure rise coefficient. Furthermore it was demonstrated above, that the mass flow and area averaged total pressure rise coefficients are almost identical at rotor speeds below rotating stall inception. After inception, the results of mass-flow averaging and area averaging differ but the apparent differences may be a result of errors in the axial velocity data derived from triple probe measurements in the presence of rotating stall. The area-averaged total pressure rise data may be more reliable after rotating stall inception. Thus, it is of interest to examine the rotor losses calculated from the torque coefficient and the area-averaged total pressure rise across the staged rotor. The results are presented in Figs. 18, 19 and 20 for the three stator stagger angles tested. For the staged rotor, the integrated data in these figures are averages of the two sets of total pressure distributions measured for each rotor speed.

Each of Figs. 18, 19 and 20 presents the torque coefficient, the area-averaged total pressure rise across the rotor and the relative losses calculated from the first two quantities. Similar quantities measured on the isolated rotor are shown as dashed lines for comparison. The lowest rotor speed at which rotating stall was present during the measurements is denoted by arrows on each figure.

At the lowest stator stagger angle (Fig. 18), the area-averaged total pressure rise across the isolated rotor and staged rotor are almost identical up to a rotor speed of 700 RPM. As rotor speed is increased further, the staged rotor displays a progressively larger overall total pressure rise until it enters rotating stall. After stall inception, the staged rotor total pressure rise becomes less than that for the isolated rotor. As can be seen in the radial distributions of Fig. 13, the drop in overall total pressure rise after rotating stall inception on the staged rotor is due to the suddenly large deficits near the tip region. The region near the hub retains a large surplus in total pressure rise.

As the stator stagger angle is increased (Figs. 19 and 20), the increased total pressure rise across the isolated rotor extends to lower rotor speeds until at the lowest stator stagger angle (Fig. 20), there is a moderate increase even at the lowest rotor speeds. After rotating stall inception on the staged rotor, the total pressure rise on the staged rotor for these stator stagger angles also drops to values less than that found on the isolated rotor; although the deficit decreases as the stator stagger angle increases.

In general, the area averaged total pressure results on this low hub-to-tip ratio configuration do not display as large an effect of rotor-stator interference as that found on the high hub-to-tip rotor configuration. On the latter, the addition of a stator row increased the rotor total pressure rise coefficient by a value of approximately 0.2 at low rotor speeds and 0.4 to 0.5 just prior to stall inception on the isolated rotor (Ref. 3, Fig. 7). The corresponding numbers in Figs. 18, 19 and 20 are 0 to 0.05 at low rotor speeds and approximately 0.1 to 0.2 just prior to inception on the isolated rotor. After inception the two configurations are not comparable; the high hub-to-tip ratio stage entered a full-span large amplitude rotating stall with hysteresis while the current configuration entered rotating stall progressively with a part-span small-amplitude stall which did not display hysteresis effects.

Comparison of the relative loss curves in Figures 18, 19 and 20 for the isolated rotor and staged rotor indicates that the increase in rotor torque

when a stator row is added downstream only partially offsets the changes in area-averaged total pressure rise across the rotor. At rotor speeds up to 700 RPM, where the rotor total pressure rise is changed very little by the addition of a stator row, the small increase in rotor torque on the staged rotor leads to calculated relative losses which are very slightly higher for the staged rotor than for the isolated rotor. This result is independent of stator stagger angle, the relative losses obtained with each stator stagger angle are identical to within the experimental accuracy in this speed range. At higher rotor speeds, but below that for rotating stall inception on the staged rotor, the relative losses at the two smaller stator stagger angles (Figs. 18 and 19) are less than those which occur on the isolated rotor. However, for the largest stator stagger angle in the same speed range, (Fig. 20), the isolated rotor and staged rotor display almost identical relative loss curves until the staged rotor stalls. Thus it would appear that prior to rotating stall inception on the staged rotor, the increase in area averaged total pressure rise across the rotor is a result of changes in both rotor torque and in relative losses. The general increase in rotor torque when the stator is added does not account completely for the observed total pressure increase prior to stall inception, except perhaps for the lowest stator stagger angle tested.

One other point is worth noting in the data of Figs. 18, 19 and 20. This is that the presence of rotating stall has very little effect on the rotor torque when the mean axial velocity at the inlet is held constant. The torque coefficient curves are continuous through rotating stall inception both on the isolated rotor and on the staged rotor. This is in agreement with the assumptions used previously in application of the rotating stall stability theory to prediction of rotating stall inception on the high hub-to-tip ratio stage. However it was also assumed that the torque on the staged rotor is the same as that measured on the isolated rotor. The latter assumption is not verified by these data, although the differences are small and nearly constant with rotor speed for a given stator stagger angle. Thus the slopes of the relative loss curve on the staged rotor are not changed much by this assumption. Since these slopes are the major contributor to the theoretical stability, the effect of the assumption on the past predictions of inception should be small. Stability calculations for the current low hub-to-tip ratio rotor are presented in Section II-E.

e. Tests with Inlet Distortion

In previous investigations on a high hub-to-tip ratio configuration of the annular cascade, the effect of inlet distortion on rotating stall inception was studied for both an isolated rotor and a closely coupled rotor-stator stage (Refs. 3 and 7). The isolated rotor studies included tests with stationary two- and four-lobed circumferential distortion patterns and also with the two-lobed pattern rotating about the compressor axis. On the stage, only the two-lobed distortion patterns were used. The results of these tests were surprising. On the isolated rotor (Ref. 7), stationary distortion displayed a negligible effect on rotating stall inception or its properties after inception. Rotating distortion also had little effect except when the pattern was rotated at speeds near the natural stall propagation velocity for undistorted flow. In this case, the isolated rotor incurred rotating stall at much higher flow coefficients than for the undistorted flow case. On the stage, the presence of circumferential inlet distortion caused a delay in rotating stall inception. Application of the stability theory predicted the experimental results obtained on the isolated rotor and predicted a delay in inception for the stage but the delay was not as large as that observed experimentally. Input data for the theory were estimated from steady-state data measured on the isolated rotor with distortion and from stage data without distortion.

In the current low hub-to-tip ratio configuration of the annular cascade, the effect of inlet distortion on the work performed by the staged rotor was studied briefly through rotor torque measurements. In addition, the effect of distortion on rotating stall inception was noted. The results are summarized in Fig. 21. The 180 degree circumferential distortion screen used in these tests is described in Section II B.1.

Rotor torque coefficients measured on the stage with inlet distortion are compared to those obtained on the isolated rotor and staged rotor with undistorted inlet flow in Fig. 21. Each part, (a,b,c) of Fig. 21 presents data for a different stator stagger angle. The rotor speed at which rotating stall was first detected is indicated by arrows for each case. As noted on each part of Fig. 21, inlet distortion did not have any detectable effect on rotating stall

inception on the stage. This result is similar to that observed previously in the high hub-to-tip ratio isolated rotor but not on the high hub-to-tip ratio stage, where stall inception was delayed by distortion. It is worth noting that none of the tests in the annular cascade have resulted in the promotion of rotating stall by stationary inlet distortion. These results are in contrast with the generally accepted view that inlet distortion promotes the occurrence of rotating stall and surge.

The torque coefficients in Fig. 21 display mixed results when inlet distortion is present. At the two smaller stator stagger angles, $\delta_s = 12.9$ and 22.9 degrees, the torque coefficients measured with inlet distortion appeared to follow the isolated rotor data for undistorted inflow until rotating stall is well established. However the differences in all these sets of torque data are small in this range and the results are inconclusive. Once rotating stall becomes well established on the stage ($\text{rpm} \gtrsim 1200$), the torque coefficients measured with inlet distortion become nearly identical to those measured with undistorted inlet flow to the stage. At the largest stator stagger angle, $\delta_s = 32.9$ degrees, the torque coefficients for undistorted inflow to the isolated rotor and stage show larger differences over the complete rotor speed range. In this case the rotor torque coefficients measured on the stage with inlet distortion are the same as those measured on the stage without distortion.

In summary of the above discussion, circumferential inlet distortion had no detectable effect on rotating stall inception on the low hub-to-tip ratio stage. On the stage with the largest stator stagger angle, ($\delta_s = 32.9$ degrees), the torque on the isolated rotor and rotor in the stage displayed distinct differences with undistorted inflow; in this case the rotor torque on the stage with inlet distortion was the same as that measured on the stage without distortion (Fig. 21(c)). In the stage with the smallest stator stagger angle, $\delta_s = 12.9$ degrees, the rotor torque on the stage with inlet distortion appears to follow the torque on the isolated rotor with undistorted inflow (Fig. 21(a)) until rotating stall becomes well established. However the torque differences in this case are small and the results are inconclusive. In all cases, after rotating stall becomes well established, the presence of inlet distortion had no effect on the torque coefficient for the rotor in the stage.

5. STABILITY AND POST-STALL ANALYSES

a. Application of Stability Theory

The existing rotating stall stability theory is essentially a two-dimensional theory. In previous work it has been applied to predict rotating stall inception on a high hub-to-tip ratio rotor and rotor-stator stage with excellent results (e.g., Reference 3). The use of three-dimensional data in the two-dimensional theory was effected by using data integrated across the annulus as inputs to the stability theory. On a low hub-to-tip ratio configuration, the flow parameters are much more nonuniform with radius than they are on a high hub-to-tip ratio configuration. Thus it is of interest to see how well the stability theory predicts rotating stall inception on the current configuration of the annular cascade.

The stability theory provides an expression for the damping of small disturbance in a compressor. For an isolated rotor in incompressible flow, the damping factor is given by

$$\frac{r C_I}{n U_0} = \frac{1}{2+q} \left[1 + \Delta C_{P_{TR}} + S_2^2 + S_2' (1 - S_1 S_2) - \frac{1}{2} S_1 \Delta C_{P_{TR}}' \right] \quad (12)$$

where

$$q = \frac{dn}{r} \sec \delta$$

$$d = \text{rotor chord length}$$

$$n = \text{number of stall cells}$$

$$r = \text{radius}$$

$$\delta = \text{rotor stagger angle}$$

$$S_1 = \text{relative inlet swirl to rotor } \left(= -\frac{\omega r}{U_0} \text{ for uniform inflow to rotor} \right)$$

$$S_2 = \text{relative outlet swirl from rotor, } \left(\frac{V_2 - \omega r}{U_2} \right)$$

$$U_2 = \text{axial velocity downstream of rotor}$$

V_2 = tangential velocity downstream of rotor

ω = rotor angular velocity (rad/sec)

$\Delta C_{P_{TR}}$ = relative loss across rotor

and $()'$ denotes $\frac{\partial ()}{\partial \mathcal{J}_1}$

For positive values of $\frac{rC_I}{nU_0}$ the flow is stable; rotating stall inception occurs when $\frac{rC_I}{nU_0} = 0$.

The right side of Eq. 12 has been evaluated by integration of the experimental data over the annulus to obtain the required inputs. For undistorted inlet flow, the integral relations are

$$\bar{\mathcal{J}}_1 = \frac{1}{s} \int_s \left(- \frac{\omega r}{U_0} \right) ds \quad (13)$$

$$\Delta \bar{C}_{P_{TR}} = C_T - \frac{1}{s} \int_s \left(\frac{\bar{U}}{U_0} \Delta C_{P_{T_2}} \right) ds \quad (14)$$

and

$$\bar{\mathcal{J}}_2 = \bar{\mathcal{J}}_1 - \frac{C_T}{2 \bar{\mathcal{J}}_1} \quad (15)$$

Eq. (15) relates the outlet swirl to the inlet swirl and the torque coefficient. It is equivalent to Eq. (73) of Ref. 3 which related the outlet swirl to the inlet swirl and the work coefficient (Eq. 4). The parameter, g , in Eq. (12) is a constant for a given rotor. For the current test configuration, its value is 0.207 for $n = 1$.

The results of the stability calculations for the isolated rotor are shown in Fig. 22 where the computed damping factor is shown as a function of rotor speed. Two sets of damping factors are presented; one using relative losses calculated from the mass-flow averaged total pressure rise, (Eq. (8)),

and one in which the area averaged total pressure rise (Eq. 5), was used in Eq. (8) to compute $\Delta \overline{C_{P_{TR}}}$. As expected from the discussion in Section II.C.4 there is very little difference in the damping factors computed by mass-flow averaging and area averaging of the total pressure rise coefficients. Theoretical rotating stall inception occurs when the damping factor first goes to zero. The state of the experimentally observed rotating stall is noted as a function of rotor speed in the lower portion of the figure. Theoretical inception is predicted at a rotor speed in a range where it is possible that a very small amplitude rotating stall began to form on the rotor. Thus the agreement between theoretical and experimental inception appears to be quite good.

In addition to the stability calculations for the isolated rotor, similar calculations have been performed for the rotor in the stage. The results are presented in Figs. 23, 24 and 25 for the three stator stagger angles used in the tests. Figure 24 shows results only for the case of area-averaging the rotor total pressure rise coefficient. The velocity data required for mass-flow averaging are not available for this case. Figures 23 and 25 present results for both types of averaging. As with the isolated rotor, here again there is very little difference in the damping factors computed by mass-flow averaging and area averaging of the total pressure rise coefficients. For all three stator stagger angles, predicted inception of rotating stall is in good agreement with the experimentally observed inception. Both the theory and experiment show a delay in rotating stall inception to higher rotor speeds when the downstream stator row is added with the largest delay occurring for the largest stator stagger angle (Fig. 25).

The above stability calculations were performed using data measured across the rotor in the stage. Past experience with predicting inception on a stage has indicated that the predictions are modified only slightly when the losses across the stator row are taken into account (Ref. 3). The additional stator losses delay predicted inception to rotor speeds slightly in excess

(10-25 rpm) of those predicted when only the rotor data are used. Such a predicted delay in inception would still fall within the experimental band of uncertainty in detecting rotating state on this low hub-to-tip ratio stage. Thus it appears that the stability theory is capable of predicting inception on both high and low hub-to-tip ratio stages and that extensive velocity measurements are not necessary for application of the theory. The stability calculations require only torque and area-averaged total pressure data as inputs.

b. Post-Stall Analysis of Annular Cascade Data

Day, Greitzer and Cumpsty (Ref. 6) have proposed a post-stall model based on the idea that the next axial flow in the stall cells is near zero and that the inlet total to exit static pressure rise across a stalled compressor depends only on the number of stages in the compressor. Using empirically determined values for the pressure rise coefficient and a limiting number for the extent of a stall cell, they showed good correlation for the degree of hysteresis between stalled and unstalled compressor operation. The hysteresis loop depends on throttle characteristics as well as compressor parameters. This type of result is what is required to investigate the steps needed to make a compressor recover from rotating stall once it has occurred. The work is based on empirical data obtained on numerous low-speed (incompressible flow) research compressors. In this subsection, the analysis is applied to existing data from the annular cascade to test the analytical predictions for a stage with exit conditions which differ from those of the test rigs used to develop the empirical constants in the analysis.

The basic test compressor used in Ref. 6 to develop the required empirical constants was a low speed compressor with a variable number of stages, from one to four. The exit flow was constrained by exit guide vanes so that the discharge was axial. The inlet total to exit static pressure characteristic was determined as a function of flow coefficient by throttling the discharge at constant rotor speed. The analytical development was based on experimental evidence generated primarily on this rig, and verified by application of the analysis to results from other similar test rigs. It was concluded

that if the unstalled inlet total to exit static pressure rise is known and the stall inception point is given, then the analysis can be used to predict the type of rotating stall (part-span or full-span) which will be encountered after inception and also, in the case of full span stall, to predict the point at which stall will be eliminated (stall cessation).

As part of past tests in the annular cascade facility, the hysteresis loop between stall inception and cessation on a rotor-stator stage was routinely measured under conditions of constant mean axial velocity and variable rotor speed. The static pressure rise across the stage was also measured on the hub and on the outer casing. The use of constant axial velocity and variable rotor speed corresponds to a throttle characteristic which differs from the parabolic throttle characteristic (corresponding to constant rotor speed and variable axial velocity) which was assumed in Ref. 6. Moreover, the exit flow from the stage was not constrained to the axial direction. Instead the exit flow contained considerable swirl whose magnitude depended on the stagger angle setting of the stators in the stage. The presence of the downstream swirl decreases the static pressure downstream of the stage, and thus changes the inlet total to exit static pressure characteristic under both stalled and unstalled operating conditions. Thus it is of interest to determine if the analysis can be used to predict the stalled characteristics in the annular cascade.

Figure 26 shows the inlet total to exit average static pressure coefficients, ψ_{TS} , for a rotor-stator stage of high hub-to-tip ratio in the annular cascade. Three curves are shown, each one corresponding to a different stagger angle of the stators in the stage. The mean rotor stagger angle was held constant in these tests. The parameters used in this figure are defined as follows:

$$\psi_{TS} = \frac{p_{exit(avg)} - P_{inlet}}{\rho V_b^2} \quad (16)$$

$$\phi = U_b / V_b \quad (17)$$

where P_{inlet} = inlet total pressure
 $P_{exit}(avg.)$ = average of exit static pressures measured on hub and
on outer casing of annular cascade downstream of stage
 U_0 = mean axial velocity
 V_b = rotor blade velocity at mean radius

As can be seen in Fig. 26, ψ_{TS} in the unstalled (high ϕ) region decreases substantially at constant flow coefficient, ϕ , as the stator stagger angle, δ_s , is increased. This is because the exit swirl increases and the average exit static pressure decreases as δ_s is increased.

The points of rotating stall inception and cessation are indicated for each curve in Fig. 26. At the two lower stator stagger angles ($\delta_s = 28.2$ and 37.2 deg), the stage entered large-amplitude full-span rotating stall and there was a degree of hysteresis between rotating stall inception and cessation. On the other hand, with $\delta_s = 47.2$ deg., rotating stall inception was of small amplitude and intermittent, with no hysteresis between inception and cessation. This behavior is typical of a part-span stall at inception.

The analysis of Ref. 6 is applied to the data in Fig. 26 as follows: A parabola is passed through the origin ($\psi_{TS} = \phi = 0$)^{*} and through the points of stall inception for each stator stagger angle. The parabolas through these points are given by

$$\psi_{TS} = \left(\frac{\psi_{TS}}{\phi^2} \right)_{STALL} \phi^2 \quad (18)$$

where the subscript "STALL" denotes the measured point of stall inception. The

* Taking the origin as a point on the parabola corresponds to assuming a throttle characteristic similar to that used in Ref. 6. Actually the configuration used in the annular cascade is more closely approximated by using a small negative value of ψ_{TS} at $\phi = 0$. The required negative value of ψ_{TS} cannot be determined from the data available. However, its magnitude should be quite small and should not affect the results discussed here.

intersection of these parabolas with the line $\psi_{TS} = 0.17$ is determined as

$$\phi_{.17} = \left[0.17 \left(\frac{\phi^2}{\psi_{TS}} \right)_{STALL} \right]^{1/2} \quad (19)$$

and the theoretical extent, $\lambda_{.17}$, of the stall cell at this point is found from

$$\lambda_{.17} = \frac{\phi_{unstalled} - \phi_{.17}}{\phi_{unstalled}} \quad (20)$$

where $\phi_{unstalled}$ is the value of ϕ on the unstalled compressor characteristic at $\psi_{TS} = 0.17$. If $\lambda_{.17}$ is less than 30 percent, the compressor is predicted to enter part span stall while for greater values full-span stall is predicted.

Using the above procedure, the data in Fig. 26 provides the results listed in Table 2.

TABLE 2

UNMODIFIED POST-STALL ANALYSIS OF DAY, GREITZER, AND CUMPSTY
APPLIED TO ANNULAR CASCADE DATA

Stator Stagger Angle, δ_s deg.	28.2	37.2	47.2
Flow Coeff. at Stall, ϕ_{STALL}	.500	.468	.410
Pressure Coeff. at Stall, $\psi_{TS} STALL$.211	.207	.191
Flow Coeff., $\phi_{.17}$ at $\psi_{TS} = 0.17$.449	.424	.387
Flow Coeff., $\phi_{unstalled}$, at $\psi_{TS} = 0.17$.580	.543	.439
Extent of Stall, $\lambda_{.17}$.226	.219	.119
Measured ($\phi_{cessation}$) / $\phi_{unstalled}$ at $\psi_{TS} = 0.11$.78	.79	.79

Note that $\lambda_{.17}$ is less than 0.3 for all three stator stagger angles in Table 2. Thus this procedure predicts part-span stall for all three cases. In contrast, the experimental results indicated part-span stall only for $\delta = 47.2$ deg. Full-span stall was obtained at the two lower stator stagger angles.

The analysis of Ref. 6 provides another prediction which can be applied to the annular cascade data. The analysis predicts that if full-span stall occurs, the point at which this stall will cease as the throttle is opened is determined by the value of ϕ on the unstalled performance curve at which $\psi_{TS} = 0.11$. That is,

$$\frac{\phi_{cessation}}{\phi_{unstalled \text{ at } \psi_{TS} = 0.11}} = 0.7 \quad (21)$$

The measured values of this ratio are shown in Table 2 for all three stator stagger angles. In all cases, $\phi_c/\phi_{u,11}$ is considerably greater than 0.7 which again is in disagreement with the theory as it is applied to the data in Fig. 26. Strictly speaking, this comparison should not be used for the stage with $\delta_s = 47.2$ because the theory and experiment indicate only part span stall for this case and stall inception and cessation are predicted at the same flow coefficient under these conditions. However, the fact remains that the analysis when applied to the data in Fig. 26, does not adequately predict the post-stall behavior of the stage in the annular cascade.

As noted earlier, the analysis of Ref. 6 is based on data generated in test rigs in which the exit flow is axial, while the exit flow in the annular cascade is far from axial. Thus it was felt that the analysis should be re-applied to the annular cascade data after it had been theoretically corrected to axial exit conditions. This correction can be applied to the stage data obtained with $\delta_s = 28.2$ and 37.2 degrees because the area-averaged total pressure rise, $\overline{\Delta C_{p_T}}$, across the stage is available for these cases (Ref. 3). Correction of the data to axial exit conditions is performed by assuming loss-free turning of the swirled downstream flow to the axial direction in the following fashion. The measured area-averaged total pressure rise coefficient is given by

$$\overline{\Delta C_{p_T}} = \frac{\overline{P_{T_{exit}}} - P_{T_{inlet}}}{\frac{1}{2} \rho U_0^2} \quad (22)$$

where the bars indicate area averaging across the test section annulus. With loss-free turning of the exit flow to the axial direction, the exit static pressure will be

$$p_{exit} = \bar{P}_{T_{exit}} - \frac{1}{2} \rho U_o^2 \quad (23)$$

and

$$\begin{aligned} \psi_{TS} &= \frac{p_{exit} - P_{inlet}}{\rho V_b^2} = \left(\frac{\bar{P}_{T_{exit}} - P_{inlet} - \frac{1}{2} \rho U_o^2}{\frac{1}{2} \rho U_o^2} \right) \left(\frac{U_o^2}{2 V_b^2} \right) \\ &= \frac{1}{2} \phi^2 (\bar{\Delta C_P} - 1) \end{aligned} \quad (24)$$

The results of analyzing the data in this fashion are presented in Fig. 27, for the rotor-stator stage with stator stagger angles of 28.2 and 37.2 deg. and also for the same rotor in isolation.

Note that at a given flow coefficient, the ψ_{TS} curves in Fig. 27 for the stage are substantially higher than the corresponding curves in Fig. 26 and that the maximum values of ψ_{TS} at stall reach greater values with this data presentation. Both of these factors will affect the predictions of the analysis. Proceeding with the analysis in the same way as used for Fig. 26 provides the results listed in Table 3 under the heading "High Hub-to Tip Ratio". As can be seen, the value of $\lambda_{.17}$ is greater than 0.3 for the high hub-to-tip ratio stage with both stator stagger angles. Thus the modified analysis predicts full-span rotating stall will occur at inception. This agrees with the experiments. Moreover, the flow coefficient at cessation is now predicted with an accuracy equivalent to that found in the presentation of Ref. 6. Finally, the ratio of the measured flow coefficients given at the bottom of Table 3 is considerably closer to the value of 0.7 given in Ref. 6 and presented herein as Eq. (21).

The high hub-to-tip ratio isolated rotor in Fig. 27 and Table 3 displayed a post-stall behavior different from the same rotor in the stage. In this case, experimental rotating stall inception and cessation occurred at essentially the same flow coefficient. It was very difficult to hold this

Table 3
COMPARISON OF MODIFIED POST-STALL ANALYSIS
OF DAY, GREITZER, AND CUMPSTY WITH ANNULAR
CASCADE RESULTS

PARAMETER	HIGH HUB-TO-TIP RATIO (=0.80)			LOW HUB-TO-TIP RATIO (=0.44)		
	ISOLATED ROTOR	ROTOR-STATOR STAGE		ISOLATED ROTOR	ROTOR IN ROTOR-STATOR STAGE	
STATOR STAGGER ANGLE, δ_s , deg	—	28.2	37.2	—	12.9	32.9
FLOW COEFF. AT STALL, ϕ_{STALL}	0.517	0.500	0.468	0.54 TO 0.57	0.52 TO 0.54	0.49 TO 0.51
PRESSURE COEFF. AT STALL, $\psi_{TS_{STALL}}$	0.216	0.248	0.256	0.162	0.211	0.199
UNSTALLED FLOW COEFF. AT $\psi_{TS} = 0.17$	0.605	0.626	0.610	—	0.613	0.580
UNSTALLED FLOW COEFF. AT $\psi_{TS} = 0.11$	0.684	0.702	0.675	0.652	0.688	0.697
PREDICTED EXTENT OF STALL, $\lambda_{0.17}$	0.241	0.339	0.375	—	0.25 TO 0.22	0.23 TO 0.20
PREDICTED ϕ AT STALL CESSATION	0.517*	0.491	0.473	0.54 TO 0.57*	0.52 TO 0.54*	0.49 TO 0.51*
MEASURED ϕ AT STALL CESSATION	0.52	0.517	0.486	0.54 TO 0.57*	0.52 TO 0.54*	0.49 TO 0.51*
MEASURED $\frac{\phi_{CESSATION}}{\phi_{UNSTALLED AT \psi_{TS} = 0.11}}$	NOT APPLICABLE	0.74	0.72	NOT APPLICABLE	NOT APPLICABLE	NOT APPLICABLE

*STALL INCEPTION AND CESSATION OCCUR AT SAME FLOW COEFFICIENT

isolated rotor in either a consistently stalled or unstalled condition for a long enough time to obtain data at this flow coefficient. As indicated in Table 3 for this case, the modified post-stall analysis of this case predicts an extent of stall ($\lambda_{.17}$) which is less than 0.3 and thus a part-span stall for which stall inception and cessation occur at the same flow coefficient. This result is in agreement with the experiments.

The modified analysis has also been applied to the data obtained on the low hub-to-tip ratio configuration of the annular cascade. Input data for the analysis are presented in Fig. 28. In the low hub-to-tip ratio configuration, both the isolated rotor and the rotor-stator stage entered rotating stall progressively with a part-span small-amplitude stall which grew progressively larger with decreasing flow coefficient. Since the initial occurrence of rotating stall was of very small amplitude, it was difficult to determine a distinct value of the flow coefficient for stall inception and cessation. Accordingly, Fig. 28 shows a small region of uncertainty for the flow coefficient at this point and both inception and cessation are taken to occur at the same flow coefficient.

The results of the modified post-stall analysis of the low hub-to-tip ratio data are presented on the right half of Table 3. The predicted extent of stall is less than 0.3 for the stage at both stator stagger angles. Thus the analysis* predicts the experimental results: a part span stall on the stage with stall inception and cessation occurring at the same flow coefficient. The ψ_{TS} curve for the isolated rotor never attains a value of 0.17 before stall inception. This result also is interpreted as an indication of part-span stall (Ref. 6) and is in agreement with the experiments.

* The ψ_{TS} curves for the stage in Fig. 28 are based on the total pressure rise across the rotor in the stage rather than the rise across the complete stage. Since the modified analysis used in Table 3 assumes loss free turning of the exit flow to the axial direction, it is equivalent to assuming that the downstream stator row will generate no losses. Inclusion of stator losses will lower the curves for the stage, but the predicted part-span stall would be unchanged by this effect.

In summary, the predicted results of the modified post-stall analysis agree with the experimental observations for all of the annular cascade tests. These include both low and high hub-to-tip ratio isolated rotors and rotor-stator stages. The modification to the original analysis of Ref. 6 appears to be required for exit flows which contain significant swirl. In these cases, the Ref. 6 analysis is modified by using total pressure data to calculate the downstream static pressure which would be obtained by loss-free turning of the swirled flow to the axial direction.

SECTION III

J-85 ENGINE TESTS

1. INTRODUCTION

In previous programs, a rotating stall control system for axial flow compressors was built and tested on the rotating annular cascade facility and on a J-85-5 turbojet engine (Refs. 1, 4, 13 and 14). The principle of operation of the control has been described in Ref. 1. Very briefly, the control is an electronic feedback control system which uses unsteady pressure signals produced by pressure sensors within the compressor to detect the presence of stall and provide a correction signal when stall occurs. On the J-85 engine, the correction signal is used to drive a fast-response hydraulic actuator which operates intermediate stage compressor bleed doors and inlet guide vane flaps. The performance of the stall control system was tested by closing the interstage bleed doors until rotating stall occurred or until the control anticipated stall and held the bleed doors open. The latest tests of the stall control on the J-85 (Ref. 1) showed that the stall control is capable of anticipating stall before it occurs and keeping the engine completely clear of stall at speeds up to 80 percent of design speed. No tests were performed at speeds above 80 percent of design because it was believed that opening the bleed doors at such speeds might aggravate the stall rather than clear it.

During the current program, the J-85 engine with stall control system was installed in the Ludwig tube at Calspan for blast response tests in which a shock wave is used to simulate a nuclear blast wave impinging on the engine inlet (Ref. 15). The stall control feature was not a subject of investigation in these blast response tests. One purpose of the current program was to study the stall control feature in operation under blast conditions. A second purpose was to investigate the unsteady temperature fluctuations in the J-85 compressor during the presence of rotating stall. In the process of performing the temperature measurements, additional information on the performance of the stall control system was obtained. This section presents the results of all of the J-85 tests. The results of the stall control performance tests are presented

in Section III. C., the in-stall temperature measurements in Section III. D., and the stall control blast tests in Section III. E. In addition, the post-stall analysis of Day, Greitzer and Cumpsty was applied to the J-85 data. The results of this application are presented in Section III. F. The instrumentation used on the J-85 during the tests is described first (Section II. B.).

2. INSTRUMENTATION

The instrumentation used in the J-85 compressor was similar for all of the tests. The location of the instrumentation in the compressor is shown in Fig. 29. The original J-85/stall control installation contained eight pressure transducers for stall detection purposes. These were situated at four axial locations, with two circumferentially separated transducers at each of the following locations:

<u>Axial Location (Figure 29)</u>	<u>Description</u>
(1)	near the first stage rotor mid-chord;
(2)	near the quarter-chord of the first stage stator, as close to the stator suction surface as possible;
(3)	near the trailing edge of the second stage rotor;
(4)	between the second stage stator trailing edge and the third stage rotor leading edge.

In the current program, the two pressure transducers situated at axial location No. 2 were replaced with thin film temperature probes capable of high frequency response. The configuration of these temperature probes is sketched as probe type 1 in Fig. 30. These probes each contain two thin film gauges at different radial locations. The maximum insertion distance of these probes was chosen so that they did not interfere with the first stage rotor. The probes were installed with the thin film gauges facing upstream in the compressor.

In addition to the temperature and pressure sensors at axial locations 1 through 4, the original compressor casing had provision for a monitor pressure transducer near the rear of the compressor between the seventh stage stator blades at approximately midchord (axial location 5 in Fig. 29). This pressure

transducer was also replaced with a thin film temperature probe (probe type 2 in Fig. 30). Here again, the probe was mounted with the thin film gauge facing upstream in the compressor.

It was originally planned to use a steady-state thermistor or thermocouple probe at one of the circumferential positions at axial location 2 in the compressor. This probe was to be mounted within a stagnation shield with small air bleeds so as to measure mean total temperature for comparison with the fast response thin film probes. However, it was not possible to fit such a probe within the existing constraints of the J-85 compressor geometry and instrumentation holes in the casing. As an alternative temperature probe, a thin wire temperature probe similar to a hot-wire anemometer probe was built, calibrated and tested in the compressor. This probe was unsuccessful; the thin wire broke before any data were obtained. Thus the thin film temperature probes shown in Fig. 30 were used during all tests.

In addition to the pressure transducers and temperature probes noted above, two other transducers are also installed on the engine. One of these is used to measure the static pressure rise across the compressor, and the other is used to measure the dynamic pressure at the throat of the bellmouth upstream of the compressor. This last transducer is used to provide a measure of mass flow through the compressor.

3. ROTATING STALL CONTROL TESTS

In the J-85 unsteady temperature tests which will be discussed shortly, the engine was forced into rotating stall by closing the bleed doors on the compressor. The stall control system was in operation during these tests to ensure the safety of the engine. However, the stall control was detuned so that bursts of rotating stall could be achieved. In the initial tests, the J-85 was stalled at engine speeds of 60, 65 and 70 percent of design speed with the stall control set to minimize the time that the engine remained in rotating stall. In later tests, the engine was stalled at nominal engine speeds of 70, 75 and 78 percent, and some attempts were made to stall the engine at higher speeds. The latter attempts were unsuccessful; the engine would not stall even with the bleed doors closed completely.

At each of the three largest engine speeds noted above, a number of stalls were initiated with the stall control set at progressively lower integrator gains to slow down the stall control response speed and allow progressively longer bursts of rotating stall. The slowing down process was continued until stall recovery was delayed to such an extent that a substantial uncontrolled engine deceleration occurred prior to stall recovery. The progressive lengthening of the stall duration was done primarily to ensure that the maximum effect on the unsteady temperature fluctuations during stall was obtained. However, the effect on the J-85 of slowing down the control response is of interest in its own right and is discussed in the following paragraphs.

a. Time Available to Effect Stall Recovery

The response of the J-85 engine to rotating stall at the various engine speeds and stall control response speeds is illustrated in Figs. 31 through 36. Figs. 31 through 33 are strip recorder records taken with a slow chart speed and include approximately 8 seconds of test results. Each of these figures is for a different nominal engine speed and the sub-parts (a, b, c, d) of the figures present results at progressively lower values of stall control integrator gain (and hence, slower stall control response). Figs. 34 through 36 present essentially the same results as Figs. 31 through 33 but on a much expanded time scale which covers approximately 320 milliseconds. In each figure, six recorded traces of engine and stall control data are shown as a function of time. The time increases from left to right and the time scale is indicated just below the fifth record from the top. The recorded parameters shown in these figures have been described in Ref. 1. The descriptions are repeated below for the sake of clarity.

- (1) Engine RPM (Uncorrected) - This is a record of the engine speed in percent of design speed. It is obtained from a magnetic pick-up which counts blade passage of the first stage rotor. The record has not been corrected for compressor inlet temperature.
- (2) Bleed Door Position - This is a record of the position of a linear potentiometer on the J-85 variable geometry bellcrank. It is representative of the bleed door position as well as the configuration of the inlet guide vanes since both are connected mechanically.

- (3) Integrator Output - This is a record of the electrical output from the stall control system. A non-zero output (downward deflection on the chart) from the integrator will open the bleed doors in proportion to the magnitude of the output. A very rapid increase in the integrator output, such as when large amplitude rotating stall occurs, opens the bleed doors at a rate determined by the capability of the hydraulic actuation system. The integrator gain controls the rate at which this signal increases: the larger the gain, the faster this signal increases when stall occurs.
- (4) Compressor Static Pressure Rise, ΔP_{REF} - This is a record of the pressure difference between static pressure taps located on the outer casing upstream and downstream of the compressor. The control system pressure, P_R , is derived from ΔP_{REF} as explained in Reference 1. The bias, B, and gain, K, which determine the shape of the system reference pressure, P_R , curve (Ref. 1, Fig. 5) are noted just below the first record.
- (5) Compressor Inlet Dynamic Pressure, q_0 - This is a record of the dynamic pressure at the throat of the bellmouth upstream of the J-85 compressor. It is proportional to the square of the mass flow at the compressor inlet.
- (6) Detector Static Pressure Signal - No. 2 Stator Left - This is a record of the signal from one of the control pressure transducers mounted in the compressor outer casing. This signal along with signals from the other transducers are used by the control system to detect the presence of rotating stall. If the amplitude of the fluctuations in any one of these signals becomes larger than the system reference pressure, P_R , the control opens the bleed doors until the fluctuation amplitude decreases below the reference level. After stall disappears for a specified time (0.2 seconds in these tests), the bleed doors return to their original position. The rate at which the bleed doors return is specified

by the decay rate of the integrator in the control system. In these tests, the time constant for the decay rate was 2 seconds. The recorded signal in this record has been filtered as indicated in Fig. 3 of Ref. 1.

The vertical scales for all of the records discussed above are presented on the right side of each record. Rotating stall inception is indicated by a vertical dashed line in each figure. The position of this line corresponds to the first indication of rotating stall in either the detector pressure signals or the unsteady temperature signals. The unsteady temperature signals are not shown in these figures. They are presented later in this report.

The slow chart speed records (Figs. 31, 32, 33) illustrate the long time effect of the stall on the engine. On the left side of these figures, the bleed doors are being closed slowly. At constant throttle position this causes an increase in static pressure rise ΔP_{REF} , a small increase in engine speed, and a decrease in inlet dynamic pressure. These gradual changes are not very apparent in the figures because the lengths of the records have been shortened for presentation purposes. However, they can be seen by close inspection of Figure 31(c). At all but the lowest value of integrator gain in each of Figs. 31, 32 and 33, when rotating stall occurs the bleed doors open fast enough to allow rapid recovery from the stall. There is a significant but momentary drop in compressor static pressure rise and inlet dynamic pressure and a small temporary decrease in engine speed which occurs usually after stall recovery. After stall recovery there are also more permanent effects on the engine parameters caused by the fact that the bleed doors are now more open than they were prior to stall. The compressor static pressure rise is lower, the engine speed is very slightly lower, and the inlet dynamic pressure is higher. These are all normal effects associated with the bleed door position.

At the lowest integrator gain for each engine speed (Figs. 31(d), 32(d), 33(b)), the stall control did not open the bleed doors fast enough to prevent a significant engine deceleration prior to stall recovery. In each case,

stall recovery was not initiated until well after the bleed doors were open. While stall was occurring, the pressure drop across the compressor caused the engine to decelerate prior to stall recovery. At 71.1 percent initial corrected engine speed, Figure 31(d), the stall was relatively short (≈ 0.34 seconds) and the engine speed dropped only six percent before recovery was initiated. However, at initial corrected engine speeds of 75.5 and 78.7 percent (Figs. 32(d) and 33(b)), the length of the stall was substantial, approximately 1.9 seconds in each case. The engine recovered from both stalls at a corrected engine speed very close to 57 percent. For the stall initiated at 75.5 percent corrected engine speed (Figure 32 (d)), the operating engineer chopped the throttle to idle before recovery was completed. However, it can be seen that recovery had been initiated before the throttle was chopped. At the initial corrected speed of 78.7 percent (Figure 33(b)), the throttle was not decreased and full recovery was obtained. Subsequent tests, which are not presented here, showed similar full recovery from long duration stalls at initial engine speeds of 75 percent.

It is believed that the long duration stalls shown in Figs. 32(d) and 33(b) are quite similar to what is sometimes referred to as a non-recoverable stall or stall stagnation. In fact, if the bleed doors had not been opened by the stall control the stall recovery would not have occurred. These long duration stalls are not acceptable for an operational engine in an aircraft. A similar long duration stall was observed in Ref. 1 at 79 percent engine speed with a rate limiting device on the output of the stall control system. Tests without the rate limiter at an engine speed of 79 percent were not performed in that work. However, on the basis of trends shown by tests with and without the rate limiter at lower engine speeds, it was concluded that the stall control was not fast enough to clear stalls, once they had started without first allowing a substantial engine deceleration. The control could be set to anticipate and prevent the stall from developing, but it could not clear the stall rapidly if it did start. The current results show that the control is fast enough to clear stalls without engine deceleration at the highest speeds for which it is possible to stall the J-85 by closing the bleed doors. This is illustrated in Fig. 33(a). Attempts to stall the engine at higher engine speeds were unsuccessful, even with the bleed doors completely closed.

The above discussion raises the question of how fast a control action is required to clear stalls rapidly once they have started. A partial answer can be given by inspection of the expanded time records presented in Figs. 34, 35 and 36. The parameters in these records are the same as those in Figs. 31, 32 and 33. However, the time scale in the vicinity of rotating stall inception has been expanded 25 times.

Inspection of these figures suggests that long duration stalls were prevented when the bleed doors opened fast enough to initiate recovery within the time required for the passage of seven stall cells past the detector static pressure transducer. As will be shown later (Section III.D.1.), stall cell passage is indicated by the positive peaks in the detector record on each figure. Although successful recovery was obtained with as many as 8 or 9 cells passing the detector (Figs. 34(c), 35(c) and 36(a)), comparison of these results with the corresponding long duration stalls (Figs. 34(d), 35(d) and 36(b)) shows that stall recovery was initiated approximately at the time of passage of the seventh cell. This observation can be used to estimate the reaction speed required of the stall control system on the J-85 engine. The seventh stall cell will pass the detector in a time interval corresponding to six revolutions of the cell, since the first cell is detected at inception. Analysis of the long duration stalls shows that rotating stall on the J-85 consists of one cell rotating in the direction of the rotor at 39 to 40 percent of the rotor speed. Thus the time, T_C , available for control action is approximately

$$T_C \approx 6 / [0.4 \times (\text{ROTOR RPM} / 60)] \text{ seconds.}$$

The estimated time, T_C , is shown on the bleed door records in Figs. 34, 35 and 36. If T_C is taken as the maximum time available to open the bleed doors completely, then it can be seen that the T_C estimates are slightly conservative at nominal engine speeds of 70 and 75 percent. Unfortunately, no records were obtained for an integrator gain of 400 with an engine speed of 78 percent, and the J-85 entered a long duration stall with an integrator gain of 200 at this engine speed. Thus the adequacy of the T_C estimate is not proven in this case. However, the short duration stall at a nominal engine speed of 78 percent (Fig. 36(a)) satisfied the T_C criterion while the long duration stall (Fig.

36(b)) exceeded the T_C criterion. Moreover, the long duration stall shown in Fig. 29 of Ref. 1 also exceeded the T_C criterion. For this case, the value of T_C is 67.8 milliseconds. The bleed doors were still approximately 20 percent closed at this time.

The above estimate for the control time available to prevent long duration rotating stall is longer than that which can be inferred from the comments of Mazzawy and Greitzer in the discussion of Ref. 13. They show that the growth of a stall cell is a function of the number rotor revolutions after inception, and hence the growth scales directly with rotor speed. The graph presented in Fig. 12 of Ref. 13 shows that stall cell growth is nearly completed within 5 or 6 revolutions. Thus they conclude that preventing rotating stall becomes very difficult at high speed because of the shorter growth times of the stall cells. The estimated time, T_C , developed above corresponds to 15 rotor revolutions on the J-85 engine. The current installation of the control on the J-85 is easily capable of full action within this time period even at 100 percent engine speed (RPM = 16,560; T_C = 54 milliseconds). On the other hand, if 5 rotor revolutions are used to develop a time criterion, full control action would be required in 26 milliseconds at 70 percent engine speed and in 24 milliseconds at 75 percent engine speed. Inspection of Figs. 34 and 35 shows that this time was exceeded by a large amount prior to the onset of long duration rotating stall. Thus the comments of Mazzawy and Greitzer appear to underestimate the time available for stall control action. On the J-85 engine, the stall control is capable both of anticipating and preventing rotating stall (Ref. 1), and also of rapidly clearing stalls if they do start.

b. Stall Anticipation

As noted above, it was shown in Ref. 1 that the Calspan/Air Force rotating stall control system is capable of anticipating rotating stall on the J-85 engine and preventing its onset. However, the F.M. tape records of those tests were not long enough to allow study of the details of the control action over the long time periods prior to the inception of rotating stall or its prevention by the control system. During the current program, some pre-stall

records were obtained which are suitable for studying the anticipating capabilities of the stall control system. These records have been analyzed and the results are presented below.

Pre-stall records from two stall control tests on the J-85 engine are shown in Figs. 37 and 38. Each figure is composed of selected portions of a very long strip recorder chart. Each portion contains approximately 50 milliseconds or slightly more of data records, with large time gaps deleted between the portions to allow compression to report size figures. The total elapsed times between the start of the test (left side of each figure) and stall inception (right side of each figure) is 15 seconds for Fig. 37 and 56 seconds for Fig. 38. Fig. 37 presents results obtained with the stall control detuned to allow stall and Fig. 38 presents results with the control tuned so that stall was delayed for a considerable time.

The recorded parameters in Figs. 37 and 38 have been described in the previous subsection. A brief outline of the tests is as follows. The J-85 is stalled by closing bleed doors on intermediate stages of the compressor at engine speeds for which these doors would normally be open. The stall control uses unsteady pressure signals from pressure transducers (detectors) in the compressors to detect when rotating stall is about to occur. The amplitudes of these unsteady signals are compared to a reference level derived from the static pressure rise, ΔP_{REF} , across the compressor. When the detector signals exceed the reference level, amplitudes in excess of this level are integrated and used to provide a signal (integrator output) for opening the bleed doors. With proper tuning of the conditioning for ΔP_{REF} , the stall control reference level becomes sufficiently small to prevent the bleed doors from being closed far enough to cause inception of rotating stall (Ref. 1). If the control is detuned to allow larger reference levels, rotating stall inception will be allowed, but recovery from the stall is extremely rapid (Section III. C.1.). In order to avoid unwarranted action by the stall control system, the reference level must be larger than the background noise generated by the detectors when the engine is operating normally.

The data records in Figs. 37 and 38 display the engine speed, bleed door position, integrator output (stall correction signal) compressor static pressure rise ΔP_{REF} , dynamic pressure at the compressor inlet, and the unsteady pressure signal from one of the detector pressure transducers in the compressor. The latter signal, which is shown on the bottom record, has been amplified considerably from levels used in the previous subsection, in order to study the amplitude of the fluctuations preceding stall inception. Also shown on the bottom record is the reference level (derived from ΔP_{REF}), which is used by the control for comparison with the unsteady detector signal.* Fig. 37 shows two such levels; the one used for the test, and one which has been found to anticipate and prevent stall completely (Ref. 1) at the tested engine speed. The reference level used in the test of Fig. 38 lies between the above two values.

On the left side in Figs. 37 and 38 the engine is initially operating normally with the bleed doors fully open. Progressing to the right, an off-schedule command to close the bleed doors is applied gradually by the operating engineer. In Fig. 37, where the stall control reference level is not small enough for stall anticipation, the integrator output remains almost zero and the bleed doors close as commanded until stall inception occurs. Once this happens, the detector pressure amplitude becomes very large (off-scale) and the bleed doors open rapidly to effect recovery from the stall. As indicated by the ΔP_{REF} record, recovery is completed prior to the end of the figure. As the bleed doors are closing, the detector signal amplitude increases from values considerably less than the reference level for stall

* The detector signal is amplified and rectified within the stall control system before comparison with the reference level. The detector record shown here has not been rectified. Thus the corresponding reference level appears as upper and lower bounds enclosing the detector signal. The width between the two bounds is determined by the magnitude of ΔP_{REF} and also by the gain, K , and bias, B , used in the stall control to condition ΔP_{REF} . The values of B and K used in each test are listed in Figs. 37 and 38. The values of B and K found to provide a reference level suitable for stall anticipation (dashed lines in Fig. 37) are $B = 180$ mV, $K = 0.040$.

anticipation to values which exceed the stall anticipation reference level. The anticipation reference level is exceeded at bleed door closures of 50 percent or more while the compressor stalled at a closure of 68 percent.

The reference level used in Fig. 38 is lower than that used in Fig. 37 but not as low as that found capable of preventing stall completely. This results in substantial overriding action by the stall control system to open the bleed doors while the off-schedule command is requiring the doors to close. The position the bleed doors would have taken in the absence of stall control action has been added to the bleed door position record as a dashed line labelled "Off-Schedule Command". The time before stall inception has also been added to the lower portion of the bleed door position record. With the reference level used in this test, the stall control begins to provide a correction signal (integrator output) approximately 17 seconds before stall inception, when the bleed doors are 60 percent closed. As the off-schedule command is increased, the correction signal also increases to hold the bleed doors between 62 and 68 percent open. The compressor finally stalls at a bleed door position of 64 percent closed. This is a bit lower than the stall inception point in Fig. 37, probably because of the length of time (more than 15 seconds) that the bleed doors are held in the vicinity of the inception point.

Previous tests (Ref. 1, Fig. 32) with the reference level set at the stall anticipation level ($B = 180 \text{ mV}$, $K = 0.040$) of Fig. 37 have shown that the control will not allow the bleed doors to close more than 59 percent at the corrected engine speed (70%) corresponding to these tests. This was sufficient to avoid stall completely. As mentioned previously, the F.M. tape records of those tests are not long enough to illustrate the progressive increase of the detector signals as the bleed doors are being closed. However the current records in Figs. 37 and 38 are sufficient to illustrate the way in which stall anticipation is achieved by the control system. They also illustrate that the reference levels required for stall anticipation are high enough to avoid control action when the engine is operating normally, as on the left sides of Figs. 37 and 38.

4. THIN-FILM TEMPERATURE MEASUREMENTS DURING ROTATING STALL

These tests were designed to provide an indication of the unsteady temperatures in the J-85 compressor during the presence of rotating stall. The motivation for these tests was to determine if the presence of rotating stall can generate enough heat to ignite titanium rotor blades. It was not expected that the tests in the J-85 would display temperatures sufficient for such combustion since the compressor has a low pressure ratio and the engine would be operated at less than design speed. However, if rotating stall is a factor in titanium ignition, it was expected that a substantial increase in instantaneous temperature would be observed during the presence of rotating stall over that normally attained in the compressor.

It was not possible to measure directly the unsteady fluctuations in the air total temperature during these tests; the development of a robust, high frequency response total temperature probe was beyond the scope of the current program. Instead, thin-film gauges were mounted on probes which were inserted into the compressor just downstream of the first stage rotor and also between the seventh stage stator blades (Section III. B.). These gauges were constructed using well established techniques (Ref. 16). The thin-film gauge is made of platinum ($\approx 1000\text{\AA}$ thick) and is painted on a pyrex substrate. A coating of magnesium fluoride ($\approx 1200\text{\AA}$ thick) is vapor deposited over the gauge to protect against abrasion.

In these tests, the thin-film was used as a resistance thermometer to measure the instantaneous temperature at the surface of the pyrex substrate. The temperature-time histories from the thin film gauges can be used to determine the heat transfer rate to the probe during rotating stall and thus provide an indication of whether rotating stall might be a factor in titanium ignition in compressors. In the following presentation, the gauge temperature-time histories are presented first. This is followed by an analysis of one of these records to determine the heat-transfer rate during stall cell passage and to estimate, very roughly, the gas total temperature in the stall cell.

a. Thin-Film Temperature-Time Histories

Before entering a discussion of the thin-film data, it is appropriate to describe the differences between the probe response to slowly varying gas temperatures and to high frequency temperature fluctuations. In the case of steady flow or slowly varying flow, the probe is soaked in the flow for a sufficient time that the thin-film temperature data represent approximately equilibrium conditions; that is, the gauge data provide the steady state recovery temperature at the thin-film location. For the test conditions, this is approximately the same as the gas total temperature. For rapidly changing flow conditions, the gauge temperature-time history depends on the local heat transfer rate to the substrate and the properties of the substrate. General relations between the gauge temperature-time history and a time varying heat transfer rate are usually mathematically intractable. However, for the case of a step function increase in heat transfer rate, the gauge temperature will increase parabolically as the square-root of elapsed time (Ref. 16). A similar parabolic decrease in gauge temperature will occur if the heat-transfer rate is suddenly reduced to a lower value. As will be seen, during rotating stall the gauge temperature-time histories display the parabolic rise and fall typical of near step function changes in heat transfer rate.

Preliminary tests to obtain temperature-time histories during rotating stall were performed at engine speeds of 60, 65 and 70 percent of design speed. It was found that the temperature fluctuations during stalls at 60 percent engine speed were almost undetectable and those at 65 percent were very small (≈ 3 deg. F maximum). Thus the remainder of the tests were performed at engine speeds between 71 and 79 percent of design speed. The highest engine speed for the tests was limited by the failure of the engine to enter rotating stall at higher speeds. During the preliminary tests, the thin-film gauge between the seventh stage stators (axial location 5 in Fig. 29) failed through abrasion, presumably from small particles in the air flow. Hence, the records presented below are limited to those obtained from the four thin film gauges located just downstream of the first stage rotor (axial location 2 in Fig. 29).

The results of the thin-film temperature measurements during long duration rotating stall are shown in Figs. 39 and 40. Figs. 39(a), (b) and (c) present temperature records taken at slow chart speed for stalls initiated at 71.1, 75.5 and 78.7 percent corrected engine speed. Corresponding engine and stall control data have been presented earlier in Figs. 31(d), 32(d) and 33(b). Figs. 40(a), (b) and (c) are expanded time temperature records of the same stalls. In these cases, the corresponding engine and stall control records can be found in Figs. 34(d), 35(d) and 36(b). For reference purposes, each figure also includes a record of the static pressure fluctuations from the same stall control pressure transducer that was presented in Figs. 31 through 36. The inlet air temperature is indicated by a horizontal dashed line on each of the temperature records.

On the left side of the slow chart speed records, (Fig. 39), the temperature rises slowly as the bleed doors are gradually closed. At stall inception, the temperature rises rapidly to values significantly higher than the pre-stall temperature. At each engine speed, the largest temperature occurs just after rotating stall is initiated. After rotating stall is cleared, the temperature decreases to normal levels more gradually than the sudden increase in temperature at stall inception. The temperature behavior after stall is influenced by the after stall behavior of the engine. For the stall in Fig. 39(a), recovery was rapid (see Fig. 31(d)) and the temperatures become nearly stable over the right-hand third of the figure. In Fig. 39(b), the throttle was chopped before the engine had accelerated to its pre-stall speed (see Fig. 32(d)). In this case, temperatures are still decreasing on the right side of the figure. For the stall in Fig. 39(c), the engine had accelerated back to speed approximately 3.5 seconds after inception (see Fig. 33(b)). The temperature records become approximately stable in a similar time period.

The expanded time records in Fig. 40 show the details of the thin film temperature records just after stall inception where the highest temperatures are observed. Temperatures read from these figures are summarized in Table 4. The data obtained from the two inner gauges should be comparable since they were at the same axial location and radial immersion, but separated circumferentially by 120° . Similarly, the data from the two outer gauges should be

TABLE 4

SUMMARY OF PRE-STALL AND STALLED TEMPERATURE DATA
DURING LONG DURATION STALLS

Temperature Sensor	Engine Run 4 Test No.	Corrected Speed at Stall Inception	Pre-Stall Temp. Rise Above Inlet Air Temp. (°F)	Max. Stalled Temp. Rise Above Inlet Air Temp. (°F)	(Max. Stalled) (Temp. Rise) (Pre-Stall) (Temp. Rise)
No. 1 Stator Top,	7	71.1	34.2	59.5	1.74
Inner Gauge	10	75.5	37.8	68.6	1.81
(Immersion = 1.2 in.)	11	78.7	36.9	75.8	2.05
No. 1 Stator Top,	7	71.1	39.4	60.6	1.54
Outer Gauge	10	75.5	42.9	68.5	1.60
(Immersion = 0.6 in.)	11	78.7	43.5	75.3	1.73
No. 1 Stator Left,	7	71.1	32.4	58.1	1.79
Inner Gauge	10	75.5	35.0	66.0	1.89
(Immersion = 1.2 in.)	11	78.7	39.5	78.4	1.98
No. 1. Stator Left,	7	71.1	40.7	63.5	1.56
Outer Gauge	10	75.5	43.3	71.5	1.65
(Immersion = 0.6 in.)	11	78.7	45.9	78.5	1.71

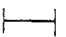
comparable. As can be seen, the data are reasonably consistent. In particular, the ratios of the maximum stalled temperature rise to the pre-stall temperature rise agree fairly well.

The largest source of error in the thin film temperature data is caused by erosion of the thin film temperature gauges during a test run. The temperature is determined from these gauges by measuring the change of resistance which is a linear function of temperature in the range of interest. Repeated calibrations of the gauges showed that the slope of the temperature versus resistance calibration did not change during a test run, but the overall level of the resistance increased. The result of the gradual increase in overall probe resistance is that the records accurately reflect short term temperature difference, but the determination of the temperature level above ambient requires correction to account for the gradual increase in gauge resistance caused by erosion. Such a correction has been made to the data presented in Figs. 39 and 40 and in Table 4. In the figures, the correction affects the position of the dashed line labeled inlet air temperature. In the table, the correction affects the overall temperature levels, but not the difference in temperature between the pre-stall condition and the maximum stalled temperature. The reasonable agreement in Table 4 between the temperature data from the two inner gauges and, separately, between the temperature data from the two outer gauges indicates that the erosion correction was fairly successful.

The data in Table 4 show that the thin-film temperatures taken just downstream of the first stage rotor during stall reach significant multiples of the steady-state pre-stall temperature rise across the rotor. The magnitude of the gauge temperature increases with engine speed and varies with radius inside the compressor. The maximum gauge temperature was observed on the inner radius gauges at an engine speed of 78.7 percent. As discussed earlier, the parabolic sawtooth nature of the temperature records indicate that the gauges were responding to nearly-step function changes in heat transfer rate during cell passage. This suggests that the gas flow temperature during stall is a nearly square wave in time with perhaps a substantially larger amplitude than that displayed by the thin film gauges. An analysis based on the square wave assumption

is presented in the next subsection and the predicted results are compared to the temperature time history obtained from one of the inner radius gauges at an engine speed of 78.7 percent.

The data presented thus far do not determine whether the high temperature regions lie within the stall cells or within the high velocity region between the stall cells. To resolve this question, the J-85 was reinstrumented with a new probe containing a thin-film gauge and a total pressure transducer. The thin film gauge was located at the radial immersion of the previous outer gauges (0.6 inch) and a total pressure tube connected to an external, closely coupled, transducer was located at the radial immersion of the previous inner thin film gauge. The J-85 was then stalled as in the previous tests. The results from a long duration stall with this instrumentation are presented in Fig. 41

The data records shown in Fig. 41 are similar to those presented in Fig. 40 except that the total pressure record replaces one of the temperature records on the probe labelled No. 1 Stator Left. The passage of stall cells past this probe is indicated by the irregular valleys in the total pressure record. The regions of increasing temperature on the thin film gauge on the same probe are indicated by . These same regions have been transferred to the total pressure record and to the detector static pressure record. It can be seen that the rising temperature region on the thin film record correlates very well with stall cell passage as indicated by the total pressure record. These increasing temperature portions of the thin film records correspond to the high temperature regions in the gas flow. Thus it is concluded that the highest temperatures during rotating stall occur within the stall cells. This indicates that the work input by the rotor remains large during stall cell passage and that it is transformed primarily to heat. The large work input during stall has also been suggested by previous low speed annular cascade experiments (Ref. 3) and by the torque measurements presented in Section II.

One final observation on Fig. 41 is relevant to the previous discussion on the time available for the stall control system to initiate rapid stall recovery (Section III.C.1.). It was stated in that discussion that the positive peaks in the detector static pressure record correspond to the passage of stall cells past the detector transducer. This transducer is at nearly the same circumferential location and only slightly displaced axially from the total pressure probe in Fig. 41. Thus, stall cells pass both of these transducers at nearly identical times. Comparison of the total pressure and detector static pressure records in Fig. 41 shows that the positive peaks in the static pressure record do serve as an indication of stall cell passage as stated earlier. However, the amplitude and phase of the detector static pressure record have been modified by filters in the stall control system (see Ref. 1, Fig. 6). Thus, this record should not be used to obtain quantitative static pressure data.

b. Analysis of Temperature Records

In the preceding discussion, it was noted that the parabolic sawtooth shape of the thin film temperature records suggested a square wave variation of heat-transfer rate with time. An analytical model based on this assumption is sketched in Figure 42. With this assumed model, the expression for the time dependence of the thin film gauge temperature becomes

$$T(t) - T(0) = \frac{2}{\sqrt{\pi k_s \rho_s c_p}} \left\{ A \left[\sqrt{t} - \sqrt{t-t_1} + \sqrt{t-t_2} - \sqrt{t-t_3} + \dots \right] \right. \\ \left. + B \left[\sqrt{t-t_1} - \sqrt{t-t_2} + \sqrt{t-t_3} - \sqrt{t-t_4} + \dots \right] \right\} \quad (25)$$

where $T(t)$ = thin film temperature ($^{\circ}\text{F}$)
 A = heat transfer rate during stall cell passage ($\text{BTU}/\text{ft.}^2\text{sec}$)
 B = heat transfer rate between stall cells ($\text{BTU}/\text{ft.}^2\text{sec}$)
 k_s = thermal conductivity of substrate ($\text{BTU}/\text{ft. sec. } ^{\circ}\text{F}$)
 ρ_s = density of substrate ($\text{slug}/\text{ft.}^3$)
 C_{p_s} = specific heat of substrate ($\text{BTU}/\text{slug } ^{\circ}\text{F}$)
 t = time after stall inception (sec.)
 t_i = time's associated with stall cell passage (Figure 42)
 i = 1, 2, -----

For the pyrex substrate used in the thin film gauges, Reference 16 gives

$$\frac{1}{2} \sqrt{\pi k_s \rho_s C_{p_s}} = 0.066 (\text{BTU}/\text{ft.}^2 \text{ } ^{\circ}\text{F. sec}^{1/2})$$

Typical temperature response curves for B equal to three fractional values of A are sketched at the top of Figure 42. The predicted response curves appear quite similar to the experimental data presented in Figure 40. Thus, a short parametric study was made to fit the predicted response to one of the experimental thin-film gauge records.

The results of the best fit predicted curve are compared to the experimental record in Figure 43. The experimental data were read from the record labelled "No. 1 Stator Left: Inner Gauge" in Figure 40 (c), and time $t = 0$ was taken at the first indication of gauge temperature rise due to stall cell passage. The assumed extent of the stall cell, passage time between stall cells, and heat transfer rates during stall cell passage and between stall cells are listed at the top of Figure 43. It can be seen that the simple analytical model agrees quite well with the experimental data. Thus, it would appear that an approximately constant heat transfer rate of $26 \text{ BTU}/\text{ft.}^2\text{sec}$ occurred at the thin film gauge during stall cell passage and near zero heat transfer rate occurred between stall cells.

The heat transfer rate during stall cell passage is not sufficient by itself to determine the gas temperature within the stall cell. However, a rough estimate of the minimum gas temperature can be made. For a circular cylinder, steady state data are available (e.g. Reference 9) which relate the mean Nusselt number N_m to the Reynolds number of the cylinder, R , where

$$N_m = hD/k$$

$$R = UD/\nu$$

and

D = cylinder diameter

h = heat transfer coefficient

k = conductivity of air

U = free stream velocity

ν = kinematic viscosity of air

For the steady flow case, the heat transfer rate, \dot{q} , is given by

$$\dot{q} = h(T_w - T_\infty)$$

where T_w is the wall temperature and T_∞ is the air temperature at a large distance from the cylinder. For the unsteady model considered above, it is assumed that $\dot{q}(t)$ during stall cell passage can be taken as

$$\dot{q}(t) = h(T_a(t) - T_w(0))$$

where $T_a(t)$ is the air total temperature in the stall cell at time t , and $T_w(0)$ is the wall temperature just prior to passage of the first stall cell.

The value of the heat transfer coefficient, h , is determined from the steady state data as a function of Reynolds number with appropriate values of D , k , and ν for air at approximately one atmosphere and 100 deg. F, viz

$$D = 0.2 \text{ in.} = 1/60 \text{ ft.}$$

$$k = 4.3 \times 10^{-6} \text{ BTU/ft. } ^\circ\text{F. sec}$$

$$\nu = 1.9 \times 10^{-4} \text{ ft}^2/\text{sec}$$

With these values

$$R = \frac{UD}{\nu} = 88U$$

$$h = \frac{N_m k}{D} = 2.6 \times 10^{-4} N_m$$

$$T_a(t) - T_w(o) = \dot{q}(t)/h$$

where $\dot{q}(t)$ is approximately 26 BTU/ft.²sec. during stall cell passage. Using these relations and the empirical curve in Reference 9 (p. 324) between N_m and R one obtains the following results for assumed values of velocity, U , in the stall cell.

U (ft./sec)	R	N_m	$h \left(\frac{\text{BTU}}{\text{ft}^2 \cdot ^\circ\text{F} \cdot \text{sec}} \right)$	$T_a(t) - T_w(o)$ (deg.F)
100	8,800	50	0.013	2000
300	26,400	100	0.026	1000
600	52,800	150	0.039	670
900	79,200	200	0.052	500

The above values are based on a mean Nusselt number averaged over the cylinder. Local Nusselt number at specific circumferential locations on the cylinder approach values which are two times as large as the mean value at Reynolds numbers on the order of 40,000 (Ref. 9, p. 325). Hence the temperature differences indicated above may be lower by a factor of two. Thus the above calculations suggest a minimum temperature rise in the stall cell on the order of 250 degrees F and the temperature may be much higher if the velocity in the cell is low. However, there is evidence (Reference 10) that the circumferential component of velocity in the cell can approach the rotor wheel speed so the higher values of U assumed in the calculation are not unreasonable.

An independent estimate of the temperature in the stall cell can be obtained by assuming that the rotor torque remains unchanged during passage through a stall cell and passage through the free-stream between stall cells and that the magnitude is equal to that occurring just prior to stall inception. Prior to stall inception, the torque, τ_p at a given spanwise location on the first stage rotor is

$$\tau_p = \rho U r (W_1 - W_0) \quad (26)$$

where r = radius
 U = axial velocity
 W_0 = circumferential velocity upstream of rotor
 W_1 = circumferential velocity downstream of rotor
 ρ = density

In addition the difference in air total temperature upstream and downstream is given by

$$T_{T1} - T_{T0} = \frac{\omega r (W_1 - W_0)}{C_p} \quad (27)$$

where C_p = specific heat at constant pressure
 ω = rotor angular velocity

Combining Equations (26) and (27) gives

$$(T_{T1} - T_{T0})_p = \frac{\omega \tau}{C_p \rho_p U_p}$$

If the torque is assumed constant as noted above, then

$$(T_{T1} - T_{T0})_s = \omega \tau / C_p \rho_s U_s$$

$$(T_{T1} - T_{T0})_u = \omega \tau / C_p \rho_u U_u$$

where the subscript p denotes conditions prior to stall, the subscript s denotes conditions in the stall cell, and the subscript u denotes conditions in the free stream area between cells.

For constant ω and neglecting density changes, one has

$$U_p (T_{T1} - T_{T0})_p \approx U_s (T_{T1} - T_{T0})_s \approx U_u (T_{T1} - T_{T0})_u \quad (28)$$

For zero heat transfer rate between stall cells,

$$(T_{T1} - T_{T0})_p = (T_{T1} - T_{T0})_u$$

which indicates

$$U_p \approx U_u$$

If the extent of the stall is 1/3 as used in the previous model, then the mean axial velocity, \bar{U} , during stall is

$$\begin{aligned} \bar{U} &= \frac{1}{3} U_s + \frac{2}{3} U_u \\ &\approx \frac{1}{3} U_s + \frac{2}{3} U_p \end{aligned}$$

and

$$\frac{\bar{U}}{U_p} \approx \frac{1}{3} \frac{U_s}{U_p} + \frac{2}{3}$$

Analysis of the inlet dynamic pressure record for the stall at 78.7 percent speed gives

$$\frac{\bar{U}}{U_p} \approx 0.72$$

Thus

$$\frac{U_s}{U_p} \approx 3 \left(\frac{\bar{U}}{U_p} - \frac{2}{3} \right) = 0.15$$

Finally from Equation (28),

$$(T_{T1} - T_{T0})_s \approx \frac{U_p}{U_s} (T_{T1} - T_{T0})_p$$

and from Table 4, $(T_{T_1} - T_{T_0})_p = 39.5$ deg. F for the thin film record analyzed previously. Thus, $(T_{T_1} - T_{T_0})_s = 39.5/0.15 = 263$ deg. F and the total temperature rise in the stall cell is $263 - 40 = 223$ deg. F.

This estimate is in reasonable agreement with the minimum temperature rise of 250 deg. F estimated previously from the heat transfer model. It is worth noting that the assumption of constant rotor torque implies that the product of axial velocity U and swirl velocity W is nearly constant inside and outside of the stall cell (see Equation 26). This indicates that swirl velocities inside of the cell are large, in agreement with the observations of Reference 10 and also in agreement with the high velocities used in the previous analysis to obtain a minimum value of temperature rise in the cell.

In summary, the thin film gauge temperature measurements indicate that the total temperature in the stall cell is much larger than the total temperature between cells. Estimates of the total temperature in the cells for a stall at 79 percent engine speed suggest values approximately 6 to 7 times the pre-stall total temperature rise across the first stage rotor. No data were obtained at other locations in the compressor. However, the data obtained on the first stage of this relatively low pressure ratio compressor suggest that very much higher temperatures may be reached in later stages of a modern high pressure ratio compressor at near design speeds. If such is the case, then rotating stall could be a factor in titanium combustion in such compressors. Further tests with more extensive instrumentation designed to study this phenomenon would appear to be well worthwhile.

5. STALL CONTROL BLAST TESTS

These tests are designed to study the performance of the stall control system in response to an impinging shock wave. The J-85 engine is operated at speeds for which the stall control is effective and the bleed doors are closed to a position just prior to that which induces rotating stall. The engine is then subjected to a shock wave to determine the performance of the stall control system. The impinging shock waves were generated by the Ludwig

tube at Calspan. Details of the J-85 installation in the Ludwig tube are presented in Reference 15. A sketch of the installation and the shock tube instrumentation is shown in Figure 44. The shock tube upstream of the J-85 bellmouth was instrumented with nine static pressure transducers. In the following discussion, the transducer denoted as P_9 is used to determine shock overpressure. The instrumentation on the J-85 compressor has been described previously.

In all, nine shock tests were performed at nominal engine speeds of 60 and 65 percent. Four tests were done with the control on and the bleed doors partially closed, and four similar tests were done with the control off. Finally, one reference test was performed with the engine in its normal configuration, that is with the bleed doors fully open. None of the shock tests induced rotating stall in the compressor; at a given engine speed, the compressor response to the shock wave appeared to be unaffected by the position of the bleed doors at the time of shock impingement. However, the tests with the stall control active showed that the control responds rapidly to an incident shock. This is illustrated in Figure 45.

The data presentation in Figure 45 is similar to that used in the rotating stall tests presented in Figures 34 through 36. However, in this case the disturbance is a shock wave with an overpressure of approximately 2.6 psi. The shock tube static pressure, P_9 , just upstream of the engine bellmouth has been used to determine the arrival time of the shock at the compressor bellmouth. This is shown as a vertical dashed line through all of the strip chart records.

Figure 45 shows that the bleed doors began to open within about 7 or 8 milliseconds and were fully opened in about 28 milliseconds. The results correspond approximately to the maximum response rate obtainable with the hydraulic/mechanical system used to operate the bleed doors on the J-85. This is the result that was expected from these tests. However, similar tests with the control turned off and the bleed doors closed the same amount throughout the shock passage, failed to excite a rotating stall in the compressor. In both tests the bleed door closure was approximately 4 to 8 percent less than

the average closure required to excite spontaneous inception of rotating stall. Apparently the J-85 engine is highly stable in the presence of an incident shock, even when the bleed doors are closed to a position just slightly less than that required for spontaneous inception. With the exception of the bleed door position, the test results with the control turned off were virtually indistinguishable from those shown in Figure 45 for the control turned on.

In view of the apparent stability of the J-85 compressor to incident shock waves no further shock tests were performed. The results have shown that the stall control responds at its maximum rate to an incident shock wave but it has not been shown that this response is sufficient to prevent rotating stall if the shock were to excite such stall. It is worth noting that none of the shock wave tests, including those performed under the separate blast wave program presented in Reference 15, have excited rotating stall in the J-85 engine.

Reference 15 reports the results of detailed experiments performed to investigate the behavior of a turbojet engine when subjected to a blast-wave environment. All of the experiments reported in that document were performed for sea level conditions with the stall control inactive. In order to investigate the influence of a blast wave on J-85 engine performance at conditions other than sea level, during this program the engine was allowed to pump down the test section to a static pressure approximately 2 psi lower than ambient. At this reduced inlet pressure, but with ambient exhaust conditions, shock waves were directed into the engine with the stall control inactive.

Experiments were performed for shock overpressure values up to approximately 2.5 psi at engine speeds near 95%. The dynamic engine pressure results were similar to those obtained for sea level operation. No evidence of rotating stall or surge could be found in the recorded pressure histories. These experiments were not continued beyond the exploratory results noted above because the capability of simultaneously reducing the exhaust pressure was not available.

6. POST-STALL ANALYSIS OF J-85 DATA

In Section II, the post-stall analysis of Ref. 6 was applied to the low-speed annular cascade data to test the analytical predictions for stages with exit conditions which differ from those in the test rigs used to develop the empirical constants. It was found that the analysis, modified slightly to account for the different exit conditions, provided satisfactory predictions of the experimental results. However, both the annular cascade data and the data used in Ref. 6 were obtained on low speed rigs with essentially incompressible flow. The records obtained during the long duration rotating stalls on the J-85 engine provide a source of in-stall and stall recovery data for an aircraft compressor operating in the compressible flow regime. Thus it is of interest to analyze these data to determine if the stall recovery point can be estimated by the analytical approach of Ref. 6.

The data required for application of the analysis are curves of the unstalled inlet total to exit static pressure rise coefficient, ψ_{TS} , as a function of flow coefficient, ϕ . These curves were calculated from compressor maps for the J-85 presented in the usual manner, that is, total pressure ratio, P_3/P_2 , versus corrected weight flow, $w\sqrt{\theta}/\delta$, for constant values of corrected speed, $N/N^*\sqrt{\theta}$.

Recall that ϕ and ψ_{TS} are defined as

$$\phi = \bar{U}/V_b$$

$$\psi_{TS} = \frac{P_{exit} - P_{inlet}}{\rho V_b^2}$$

where

$P_{T_{inlet}}$	=	compressor inlet total pressure (P_{T_2})
P_{exit}	=	compressor exit static pressure (p_3)
\bar{U}	=	mean axial velocity
V_b	=	rotor blade velocity at mean radius
ρ	=	air density

The following assumptions were made in calculating ϕ and ψ_{TS} .

- The mean radius is calculated at the leading edge of the first stage rotor.
- The mean axial velocity, inlet axial Mach number, and air density are calculated at the same axial location as the mean radius.
- Inlet total pressure equals ambient static pressure.
- The compressor exit axial Mach number is equal to the inlet axial Mach number. (Deviations in the real conditions from this assumption have only a weak effect on the calculated results.)

With the above assumptions, the following results are obtained:

$$\phi = \frac{60 (W \sqrt{\theta} / \delta)}{2 \pi g \rho_s \bar{R} A_2 N_2^* (\rho_2 / \rho_a) (N / N^* \sqrt{\theta})}$$

$$\psi_{TS} = \frac{\rho_s \left[\left(\frac{p_3}{p_{T3}} \right) \left(\frac{p_{T3}}{p_{T2}} \right) - 1 \right]}{\rho_s \left(\frac{2 \pi}{60} \bar{R}_2 N^* \right)^2 \left(\frac{\rho_2}{\rho_a} \right) (N / N^* \sqrt{\theta})^2}$$

$$\rho_2 / \rho_a = \left(1 + \frac{M_2^2}{5} \right)^{-5/2}$$

$$p_3 / p_{T3} = \left(1 + \frac{M_2^2}{5} \right)^{-7/2}$$

and

$$M_2 = \frac{(W \sqrt{\theta} / \delta)}{g \rho_s a_s A_2} \left(1 + \frac{M_2^2}{5} \right)^3$$

where

- a_s = speed of sound at standard conditions (1117 ft/sec)
- A_2 = annulus area at first stage rotor face (1.063 ft)
- g = acceleration of gravity (32.2 ft/sec²)
- M_2 = axial Mach number at first stage rotor face
- N = engine rpm
- N^* = engine design rpm (16,560)
- p_s = standard atmospheric pressure (2116 pounds/ft²)
- p_3 = compressor exit static pressure
- P_{T_2} = compressor inlet total pressure
- P_{T_3} = compressor exit total pressure
- \bar{R}_2 = mean radius at first stage rotor face (0.515 ft)
- ρ_2 = air density at first stage rotor face
- ρ_a = ambient air density
- ρ_s = standard atmospheric density (0.00238 slugs/ft³)

For $M_2 < 1$, the equation for M^2 can be approximated by taking

$$\left(1 + \frac{M_2^2}{5}\right)^3 \approx \left(1 + \frac{3}{5} M_2^2\right)$$

which gives

$$M_2 \approx \frac{\sqrt{1 - 2.4 K^2}}{1.2 K}$$

where

$$K = (W\sqrt{\theta}/\delta) / g \rho_s a_s A_2$$

The approximation for M_2 is within about 1 percent of the true value for the J-85 operating at 100 percent of design speed. At lower speeds, the approximation becomes more accurate.

Curves of ψ_{T_3} versus ϕ were calculated from the J-85 compressor map and the results are presented in Figs. 46(a,b,c) for a number of corrected

engine speeds. The performance maps in each part of Fig. 46 are identical; they serve as a base for presenting the J-85 data taken from the records of long duration stalls during the current program.

The data available from the records of the long duration rotating stalls are the engine speed, the total pressure, P_{T1} , minus static pressure, p_1 , in the constant diameter duct upstream of the compressor bullet nose (axial station 1), and the static pressure rise across the compressor, $\Delta p = p_3 - p_1$.

The coefficients ψ_{TS} and ϕ were calculated from these data as follows:

$$\psi_{TS} = \frac{[\Delta p - (P_{T1} - p_1)]}{\rho_a \left(\frac{2\pi}{60} \bar{R}_2 N^* \right)^2 \left(\frac{\rho_2}{\rho_a} \right) \left(\frac{N}{N^*} \right)^2}$$

$$\phi = \frac{\left(\frac{A_1}{A_2} \right) \sqrt{\frac{\rho_1}{\rho_a}} \sqrt{\frac{2g_1}{\rho_a}}}{\left(\frac{2\pi}{60} \bar{R}_2 N^* \right) \left(\frac{\rho_2}{\rho_a} \right) \left(\frac{N}{N^*} \right)}$$

$$g_1 \approx (P_{T1} - p_1) \left[1 - \frac{(P_{T1} - p_1)}{\rho_a} \right]$$

$$\frac{\rho_1}{\rho_a} = \left(1 + \frac{M_1^2}{5} \right)^{-5/2}$$

$$\frac{\rho_2}{\rho_a} = \left(1 + \frac{M_2^2}{5} \right)^{-5/2}$$

$$M_1 \approx \sqrt{\frac{1}{0.7} \frac{(P_{T1} - p_1)}{\rho_a}}$$

$$M_2 \left(1 + \frac{M_2^2}{5} \right)^{-3} = \frac{A_1}{A_2} M_1 \left(1 + \frac{M_1^2}{5} \right)^{-3}$$

where the equation for M_2 is solved by iteration. The notation used above is the same as that used previously with the following additions:

- A_1 = Duct area at station 1 upstream of compressor bullet nose
(1.396 ft²)
- M_1 = Mach number at station 1
- p_1 = static pressure at station 1 (pounds/ft²)
- p_{T_1} = total pressure at station 1 (pounds/ft²)
- q_1 = dynamic pressure at station 1 (pounds/ft²)

Using the above relations, the experimental records for the three long-duration stalls presented previously were analyzed. The results are shown in Fig. 46 superimposed on the J-85 compressor map. Each part (a,b,c) of Fig. 46 presents data for a long duration rotating stall which occurred at different engine speeds.

The data points for the long duration rotating stalls correspond to several operating conditions of the J-85. The test procedure was to set the engine at a given speed and slowly close the interstage bleed doors until rotating stall inception occurred. The triangular symbols show the approach to stall as the bleed doors are gradually closed. The initial point is for the engine operating normally with the bleed doors open. As the doors are closed, the engine speeds up very slightly, the pressure coefficient increases, and the flow coefficient decreases until rotating stall occurs. Stall inception does not occur on the normal engine surge line. This line was taken from a J-85 compressor map with the bleed doors open while the current tests destabilize the engine so that it stalls below the normal surge line.

The post-stall behavior of the J-85 is denoted by slice-of-pie symbols. In keeping with the compressor map, only data obtained after the bleed doors had opened completely are included in the figures. During the post-stall time interval, the engine is decelerating spontaneously, with corresponding decreases in both mass flow and compressor pressure rise. (The numbers adjacent to the symbols give the corrected engine speed corresponding to the nearest symbol.)

The post-stall changes in engine speed, mass flow, and compressor pressure rise combine to give a clockwise hysteresis loop to the data in Figs. 46(b) and (c). The lowest speed stall, Fig. 46(a) shows very little hysteresis. There are no data available for analysis at higher and lower engine speeds; the compressor would not stall at engine speeds above 80 percent and it recovered from stall before the bleed doors were open at speeds below 70 percent.

The engine behavior after stall recovery is shown by the square symbols. In this region the engine is accelerating to the initial test condition with corresponding increases in mass flow and compressor pressure rise. Only Figs. 46(a) and (c) show a complete set of data in this region. The operating engineer chopped the throttle before the acceleration was completed for the test of Fig. 46(b).

Inspection of Fig. 46 indicates that the post-stall analysis of Ref. 6 is not applicable in its present form to the J-85. There are several points in the analysis which would require modification before it could be applied to the present data. The greatest difficulty lies in the fact that the engine decelerates spontaneously after rotating stall occurs. The deceleration combined with the fact that each constant speed line forms a different curve for ψ_{TS} versus ϕ make it impossible to estimate the recovery conditions without additional information. Moreover, the value of ψ_{TS} per stage at recovery appears to be much larger than the value of 0.11 used in Ref. 6. For the three stalls analyzed in Fig. 46, the value of ψ_{TS} per stage was very close to 0.37 just prior to recovery. This is also much larger than the value of 0.17 used in Ref. 6 to distinguish between full-span stalls with hysteresis and part-span stalls without hysteresis. Finally, using the approach of Ref. 6 to estimate

the extent of the stall cells at recovery suggests that the extent is approximately 18^{*} percent just prior to recovery rather than 30 percent as used in Ref. 6.

In summary, analysis of the post-stall behavior of the J-85 indicates that the analysis of Ref. 6 is not applicable in its present form to this case. The empirical constants used in Ref. 6 do not appear to apply to the high-speed J-85 compressor. Even if they did apply, or alternatively if values appropriate to the current tests were used, the spontaneous deceleration of the engine after rotating stall inception prevents estimation of stall-recovery conditions. Further information is required to make such an estimate. It is suggested that further experimental studies of post-stall behavior on high speed compressors be performed to refine the empirical constants for this class of compressors. These studies would best be performed under constant speed conditions. Application of the analysis to complete engines requires further development of the model to allow for the spontaneous deceleration which occurs after stall inception.

* A value of 18 percent for the extent of the stall cells at recovery was arrived at as follows. In analogy with Eqs. (20) and (21) of Section II, the extent of stall, λ_R , at recovery is defined by

$$\lambda_R = 1 - \frac{\phi_{cessation}}{\phi_{unstalled \text{ at } \psi_{TS} = 0.37}}$$

where

$$\phi_{cessation} = \phi_{Pre-recovery}$$

In Fig. 46, values of $\phi_{Pre-recovery}$ divided by 0.82 are shown plotted at $\psi_{TS} = 2.96$ (i.e., $\psi_{TS}/\text{Stage} = 0.37$). It can be seen that these points lie at approximately the position on the unstalled compressor map which corresponds to the pre-recovery engine speed. Thus, $[(\phi_{cessation})/(\phi_{unstalled \text{ at } \psi_{TS} = 0.37})] \approx 0.82$ and $\lambda_R \approx (1 - 0.82) = 0.18$. (Separate analysis of the thin film gauge records to determine apparent stall cell extent gave values of approximately 25 percent just prior to stall recovery. However, these estimates represent values at fixed spanwise locations and are very difficult to determine accurately.)

SECTION IV

SUMMARY AND CONCLUSIONS

This report presents the results of experimental studies designed to aid in the development of methods to predict the onset of rotating stall in axial flow compressors and to predict the post-stall operation and recovery characteristics of a compressor. The experiments were performed in a low-speed rotating annular cascade facility and on a J-85-5 turbojet engine. The low speed tests studied the influence of rotor-stator interference on the work performed by a rotor prior to and during rotating stall. The J-85 experiments consisted of post-stall temperature measurements in the compressor and a demonstration of stall anticipation and stall recovery on this engine with a previously developed Calspan/Air Force Rotating Stall Control in operation. In addition, some blast tests were performed on the J-85 with the stall control both operative and inoperative.

Past studies in the annular cascade had provided basic information on rotor-stator interference and input data for an existing two-dimensional stability theory for predicting rotating stall inception. These data were obtained on a configuration of the cascade with a high hub-to-tip ratio (0.80). Both an isolated rotor and the same rotor in a rotor-stator stage were tested. Correlations between theory and experiment showed that the stability theory predicts rotating stall inception quite accurately if the area-averaged steady-state loss and turning performance are known. The addition of a closely coupled stator row downstream of the rotor delayed rotating stall inception, and also provided significantly higher total pressure rise across the rotor than that observed on the same rotor in isolation. The current studies in the annular cascade were designed to investigate if the stability theory provides accurate predictions of rotating stall inception on a low hub-to-tip (0.44) rotor and stage, and also to study the increase in total pressure rise across the rotor when a stator row is added. The experiments included detailed total pressure surveys, three-component hot-film surveys to determine velocities, and measurement of the torque input to the rotor. Both an isolated rotor and a rotor-

stator stage were tested. In addition, a brief study was performed to determine the effect of circumferential inlet distortion on rotating stall inception and on the rotor torque for the rotor in the stage.

The experimental studies in the low-speed annular cascade provided the following results. Both high and low hub-to-tip ratio rotors display interference effects when coupled to a downstream stator row; the rotor in the stage produces greater total pressure rise than that obtained on the isolated rotor with the same inlet conditions. Moreover, the rotor torque is larger on the rotor in the stage than it is on the isolated rotor. The presence of rotating stall has very little effect on the rotor torque when the mean axial velocity is held constant. Prior to rotating stall inception, area averaging and mass-flow averaging of the total pressure rise distributions across the rotor provide dimensionless results which are identical to within the experimental accuracy. In this same pre-stall region, the changes in rotor torque and average total pressure rise coefficient for the rotor in the stage combine to provide averaged relative losses across the rotor which are nearly the same as for the isolated rotor. This is true even though the pre-stall radial distributions of total pressure rise across the rotor change considerably when the stator row is added. However, small differences in the relative losses across the rotor delay rotating stall inception on the stage.

The above results were obtained for undistorted inlet flow. Some additional tests on the stage were performed with 180 degree circumferential inlet distortion. The inlet distortion had no detectable effect on rotating stall inception. This result is similar to that observed previously on a high hub-to-tip isolated rotor but not on a high hub-to-tip ratio stage where stall inception was delayed by distortion. None of the tests in the annular cascade have resulted in the promotion of rotating stall by stationary inlet distortion. These results appear to contradict the generally accepted views on the effect of inlet distortion. Rotor torque measurements in the presence of inlet distortion displayed a mixed effect. For low stator stagger angles, the torque coefficients measured with inlet distortion were nearly the same as those measured on the isolated rotor for undistorted inflow until rotating stall became well established. At the largest stator stagger angle which was tested,

the torque coefficients measured on the stage with inlet distortion were the same as those measured on the stage without distortion over both the pre-stall and post-stall ranges. For all stator stagger angles, once rotating stall became well established, rotor torque on the stage with inlet distortion was the same as that found on the stage without distortion.

The experimental data obtained in the annular cascade with undistorted inflow were used to test the predictions of rotating stall inception by the two-dimensional stability theory and also the predictions of post-stall behavior by the analytical model of Day, Greitzer and Cumpsty. The stability theory performed well in predicting inception on both the low hub-to-tip ratio isolated rotor and rotor-stator stage. The stability calculations require only torque and area-averaged total pressure data as inputs; detailed velocity data do not appear to be necessary. The post-stall behavior in the low-speed annular cascade was predictable by a slightly modified version of the post-stall analytical model. The modification appears to be required for exit flows which contain significant swirl.

The blast and rotating stall tests on the J-85 engine with stall control were performed with the engine installed in the Ludwig Tube Test Facility at Calspan Advanced Technology Center. The blast tests were designed to study the response of the rotating stall control system when a simulated blast wave impinges on the engine inlet. Separate tests were performed to study the unsteady temperature fluctuations in the J-85 compressor during rotating stall, the performance of the stall control system in anticipating and preventing rotating stall, and the performance requirements for the stall control to clear rotating stall once it has started.

The J-85 tests provided the following results. In the blast tests, neither rotating stall or surge were observed for shock overpressures up to 2.5 PSI. Shock passage triggers the stall control to respond at its maximum rate. Partially destabilizing the J-85 compressor before shock impingement does not trigger rotating stall or surge at shock passage. This result is independent of control action.

In the stall temperature studies, records from thin film temperature probes downstream of the first stage rotor were obtained during rotating stall. Individual stall cell passage was evident in these records and the temperature rise during stall cell passage increases with engine speed at inception. Analysis of the thin film records for a stall initiated at 79 percent corrected engine speed indicates a heat transfer rate to the thin film probe of 26 BTU/ft²sec during stall cell passage and zero heat transfer rate between stall cells. Determination of air total temperature in the stall cells is not possible from the measured data, but a minimum temperature rise of at least 250 deg F is suggested. A separate estimate of the temperature rise in the stall cells was performed by assuming that the rotor torque is unchanged during the presence of rotating stall. An estimated temperature rise of approximately 220 deg F was obtained in this case. Both estimates indicate that the total temperature in the stall cell was about 6 to 7 times the pre-stall temperature rise across the first stage rotor in the J-85. These results, obtained on the first stage of a relatively low pressure ratio compressor, suggest that much higher temperatures may be reached in later stages of a modern high pressure ratio compressor operating at near-design speeds. If this is true, then rotating stall could be a factor in titanium combustion in such compressors.

The stall control performance tests showed that the control is capable of anticipating and preventing rotating stall on the J-85. Moreover, normal engine operation is unaffected by the presence of the stall control. If stall inception is allowed by detuning the control, the maximum time available for complete control action corresponds to 15 engine revolutions on the J-85 engine. With longer times, a fully developed rotating stall occurs which causes large engine speed losses before recovery.

Three sets of records obtained during the rotating stall tests on the J-85 were analyzed to determine if the post-stall analyses of Day, Greitzer and Cumpsty is applicable to high speed compressors operating in the compressible flow regime. The results indicate that the analysis is not applicable in its present form to this case. The empirical constants used in the analysis do not

appear to apply to the J-85 compressor. Furthermore, even if new constants appropriate to the J-85 were determined, spontaneous deceleration of the complete engine after rotating stall inception would prevent estimation of the stall recovery conditions. The analytical model requires further development to allow for this spontaneous deceleration.

REFERENCES

1. Ludwig, G.R. "Tests of an Improved Rotating Stall Control System on a J-85 Turbojet Engine" AFAPL-TR-79-2060 August 1979
2. Homicz, G.F., Lordi, J.A. and Ludwig, G.R. "Aerodynamic and Acoustic Investigations of Axial Flow Fan and Compressor Blade Rows, Including Three-Dimensional Effects" AFAPL-TR-79-2061 August 1979
3. Ludwig, G.R. and Nenni, J.P. "Basic Studies of Rotating Stall in Axial Flow Compressors" AFAPL-TR-79-2083 September 1979
4. Ludwig, G.R. and Arendt, R.H. "Investigation of Rotating Stall Phenomena in Axial Flow Compressors, Volume III - Development of a Rotating Stall Control System" AFAPL-TR-76-48 June 1976
5. Lordi, J.A., Homicz, G.F. and Ludwig, G.R. "Investigation of Rotating Stall Phenomena in Axial Flow Compressors, Volume II - Investigation of Rotor-Stator Interaction Noise and Lifting Surface Theory for a Rotor" AFAPL-TR-76-48 June 1976
6. Day, I.J., Greitzer, E.M. and Cumpsty, N.A. "Predictions of Compressor Performance in Rotating Stall" ASME Transactions, Journal of Engineering for Power Vol. 100 pp. 1-14 January 1978
7. Ludwig, G.R., Nenni, J.P. and Erickson, J.C., Jr. "Investigation of Rotating Stall Phenomena in Axial Flow Compressors, Vol. I - Basic Studies of Rotating Stall" AFAPL-TR-76-48 June 1976
8. Shaw, M.C. and Mocks, E.F. Analysis and Lubrication of Bearings McGraw-Hill 1949 Chapter 10
9. Schlichting, H. Boundary Layer Theory McGraw-Hill Fourth Edition 1960 pp. 547-550
10. Day, I.J. and Cumpsty, N.A. "The Measurement and Interpretation of Flow Within Rotating Stall Cells in Axial Compressors" Journal of Mechanical Engineering Science Vol. 20 No. 2 1978 pp. 101-114
11. Oates, G.C., et al. "The Aerothermodynamics of Aircraft Gas Turbine Engines" AFAPL-TR-78-52 July 1978
12. "Rotating Stall Investigations" Interim Technical Report Calspan Report No. 6568-A-1 April 1980
13. Ludwig, G.R. and Nenni, J.P. "A Rotating Stall Control System for Turbojet Engines" ASME Transactions, Journal of Engineering for Power Vol. 101 No. 3 pp.305-314 July 1979

14. Ludwig, G.R. and Nenni, J.P. "Tests of an Improved Rotating Stall Control System on a J-85 Turbojet Engine" ASME Transactions, Journal of Engineering for Power Vol. 102 No. 4 pp. 903-911 October 1980
15. Dunn, M.G. and Rafferty, J.M. "Nuclear Blast Response of Airbreathing Propulsion Systems: Laboratory Measurements With an Operational J-85-5 Turbojet Engine" ASME Transactions, Journal of Engineering for Power Vol. 104 pp. 624-632 July 1982
16. Vidal, R.J. "Model Instrumentation Techniques for Heat Transfer and Force Measurements in a Hypersonic Shock Tunnel" Calspan Report No. AD917-A-1 February 1956

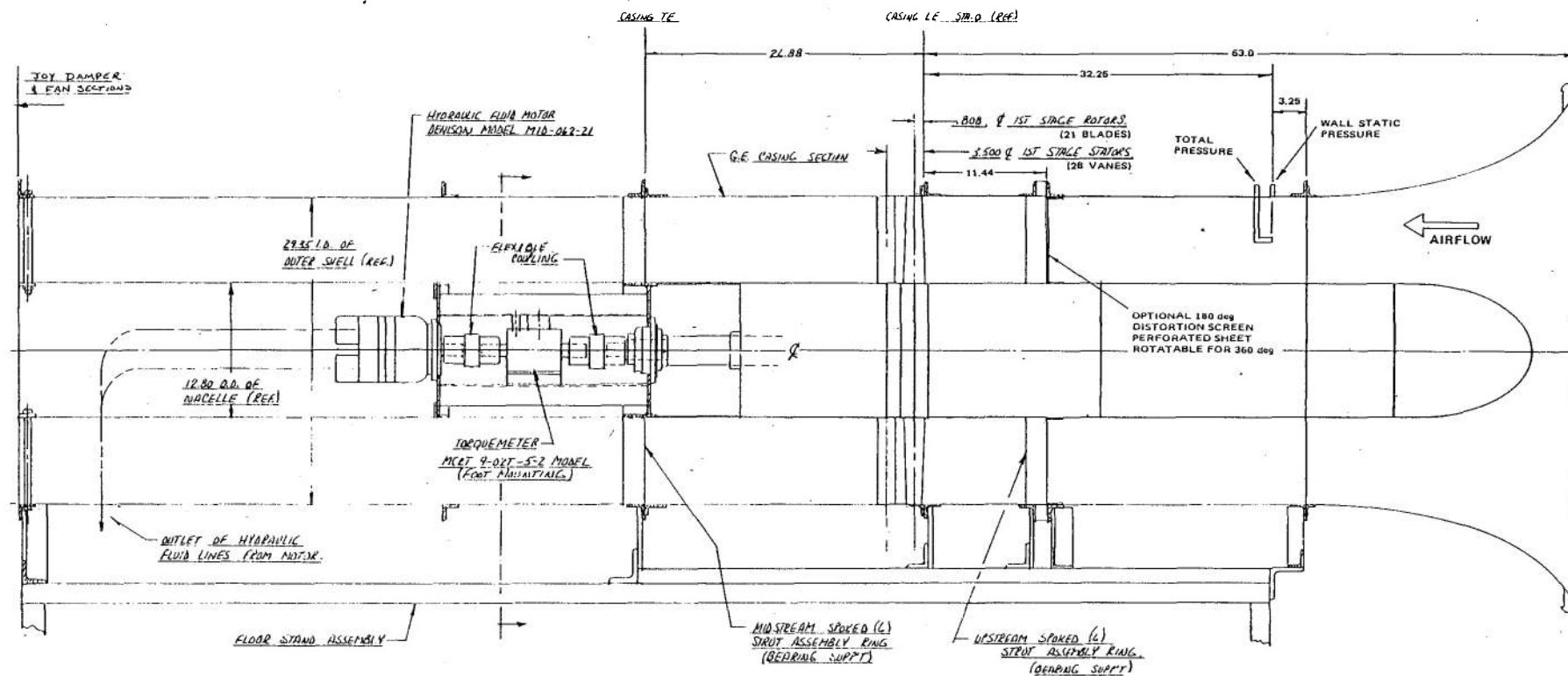


Figure 1 LOW HUB-TO-TIP RATIO ANNULAR CASCADE WITH TORQUE METER

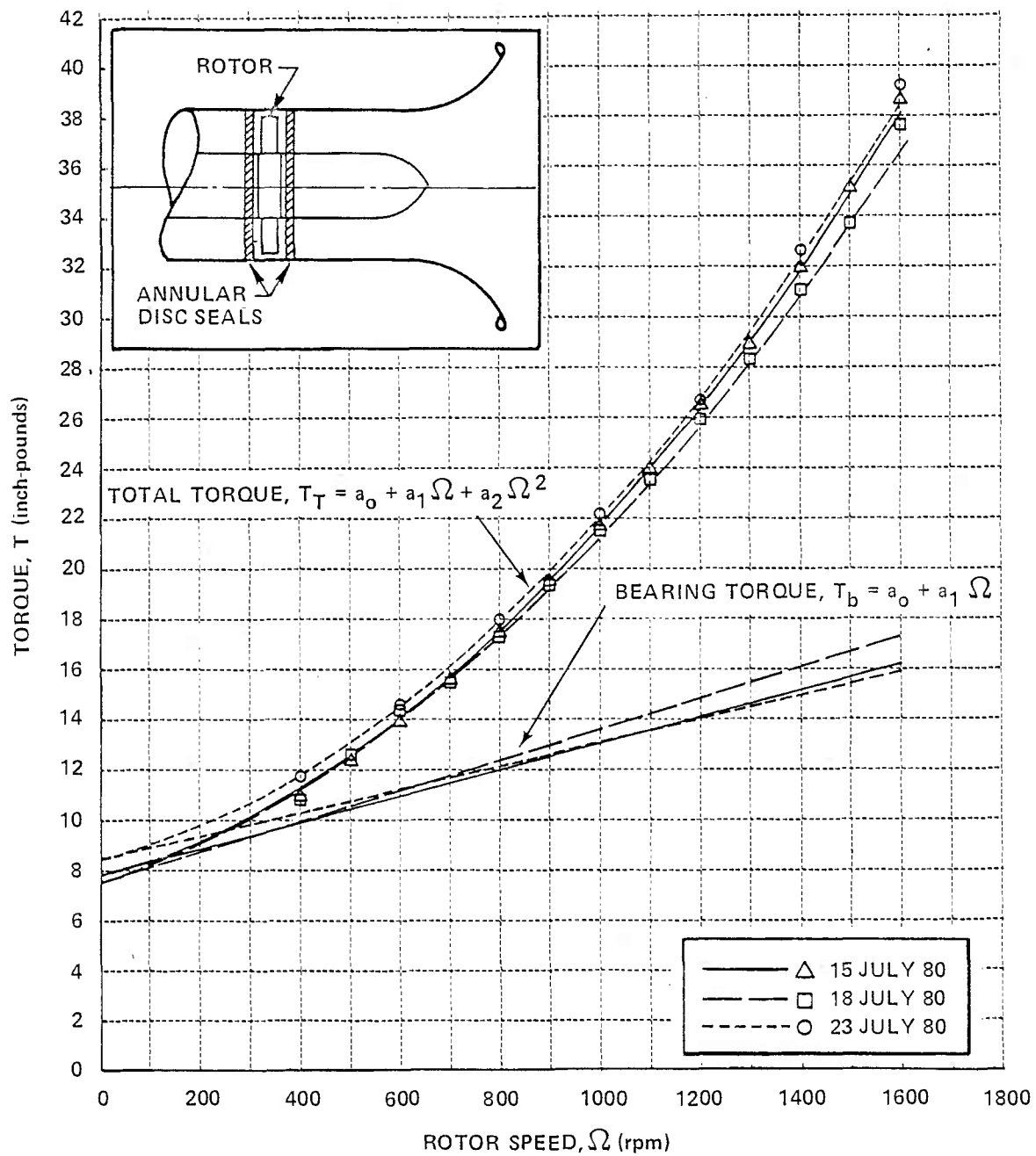


Figure 2 TORQUE ON SEALED ROTOR

